nature communications

Article

https://doi.org/10.1038/s41467-024-45081-w

Hydrogen bond unlocking-driven pore structure control for shifting multi-component gas separation function

Received: 17 January 2023

Accepted: 11 January 2024

Published online: 27 January 2024

Check for updates

Rong Yang[1,6], Yu Wang[1,6], Jian-Wei Cao[1], Zi-Ming Ye[2], Tony Pham[3], Katherine A. Forrest[3], Rajamani Krishna[4], Hongwei Chen[5], Libo Li[5], Bo-Kai Ling[1], Tao Zhang[1], Tong Gao[1], Xue Jiang[1], Xiang-Ou Xu[1], Qian-Hao Ye[1] & Kai-Jie Chen[1]

Purification of ethylene (C_2H_4) as the most extensive and output chemical, from complex multi-components is of great significance but highly challenging. Herein we demonstrate that precise pore structure tuning by controlling the network hydrogen bonds in two highly-related porous coordination networks can shift the efficient C_2H_4 separation function from $C_2H_2/C_2H_4/C_2H_6$ ternary mixture to $CO_2/C_2H_2/C_2H_4/C_2H_6$ quaternary mixture system. Single-crystal X-ray diffraction revealed that the different amino groups on the triazolate ligands resulted in the change of the hydrogen bonding in the host network, which led to changes in the pore shape and pore chemistry. Gas adsorption isotherms, adsorption kinetics and gas-loaded crystal structure analysis indicated that the coordination network Zn-fa-atz (2) weakened the affinity for three C2 hydrocarbons synchronously including C_2H_4 but enhanced the CO_2 adsorption due to the optimized CO_2-host interaction and the faster CO_2 diffusion, leading to effective C_2H_4 production from the $CO_2/C_2H_2/C_2H_4/C_2H_6$ mixture in one step based on the experimental and simulated breakthrough data. Moreover, it can be shaped into spherical pellets with maintained porosity and separation performance.

Separation of valuable components for multicomponent mixtures in one step without preconcentration is one of the most challenging tasks in separation science. In the process of C_2H_4 production, the product compositions of the thermal decomposition are complicated, and the conversion of dehydrogenation is only *ca.* 50%–60%[1]. Therefore, the resulting C_2H_4 usually contains a variety of impurities, among which carbon dioxide (CO_2), acetylene (C_2H_2) and ethane (C_2H_6) are the most difficult ones to separate because of very similar physical and chemical properties with C_2H_4[2,3]. To obtain polymer-grade C_2H_4 (>99.9%), multi-step processes are needed to remove the impurities, including chemical absorption, catalytic hydrogenation, cryogenic distillation, etc[4]. The stepwise purification processes result in huge equipment costs and energy consumption[5].

Using recyclable physisorbents, the adsorptive separation can be a promising approach for high-purity C_2H_4 thanks to the simple operation processes and lower energy requirements[6–10]. Metal–organic

[1]Key Laboratory of Special Functional and Smart Polymer Materials of Ministry of Industry and Information Technology, Xi'an Key Laboratory of Functional Organic Porous Materials, School of Chemistry and Chemical Engineering, Northwestern Polytechnical University, Xi'an, Shaanxi 710072, PR China. [2]Fujian Key Laboratory of Polymer Materials, College of Chemistry and Materials Science, Fujian Normal University, Fuzhou 350007, PR China. [3]Department of Chemistry, University of South Florida, Tampa, FL, USA. [4]Van 't Hoff Institute for Molecular Sciences, University of Amsterdam, Science Park 904, 1098 XH Amsterdam, The Netherlands. [5]Shanxi Key Laboratory of Gas Energy Efficient and Clean Utilization, College of Chemical Engineering and Technology, Taiyuan University of Technology, Taiyuan 030024, PR China. [6]These authors contributed equally: Rong Yang, Yu Wang. e-mail: ckjiscon@nwpu.edu.cn

frameworks (MOFs), or porous coordination polymers (PCPs)/metal–organic materials (MOMs), with tunable pore structures[11–15], have shown great potential for binary C2 hydrocarbons separation, such as C_2H_2/C_2H_4[16–23], C_2H_4/C_2H_6[24–31], and C_2H_2/CO_2[32–36]. Compared with the multi-step separation process, purification of C_2H_4 in one-step from complex systems is more valuable in terms of energy utilization and chemical process. However, limited by the physicochemical properties of four gas molecules (kinetic diameter: $CO_2 \approx C_2H_2 < C_2H_4 < C_2H_6$; quadruple moment: $C_2H_2 > CO_2 > C_2H_4 > C_2H_6$)[37–39], it is extremely difficult to separate C_2H_4 from the quaternary CO_2/C_2H_2/C_2H_4/C_2H_6 in one step. Although a few of studies have achieved the one-step preparation of C_2H_4 from the ternary C_2H_2/C_2H_4/C_2H_6[40–48] or more difficult four-component separation[2,49,50], the understanding of such a complex systems and the corresponding principle of structural design are far from sufficiency[51].

Herein, we show that unlocking the framework hydrogen bonding can affect the pore size/shape and pore chemistry, and weaken the affinity to C2 hydrocarbons, especially C_2H_4 (Fig. 1). The fine turning of pore structure shifts the multi-component gas separation function, enabling one-step production of high-purity C_2H_4 in the quaternary CO_2/C_2H_2/C_2H_4/C_2H_6.

Results

Structure and adsorption properties of Zn-fa-datz (1)

$[Zn_2(fa)(datz)_2]$ (Zn-fa-datz (1), H_2fa = fumaric acid, Hdatz = 1*H*-1,2,4-triazole-3,5-diamino) was initially selected[52], because of its high stability in moisture conditions (Supplementary Fig. 5), ultramicroporous nature and polar pore surface without open-metal coordination sites, based on our previously raised general rule[51]. Zn-fa-datz (1) is a pillared-layer coordination network with **pcu** topology (Supplementary Fig. 1). Each Zn^{2+} ion is saturated by three N atoms from three $datz^-$ ligands and one O atom from a fa^{2-} ligand, forming a 3D pillar-layered network with accessible 1D ultramicroporous channels (Fig. 2a and Supplementary Fig. 2). The purity and porosity were confirmed by powder X-ray diffraction (PXRD) pattern and 195 K CO_2 adsorption isotherm, respectively (Fig. 3a, Supplementary Fig. 3 and Supplementary Table 1). Note that, because N_2 diffuses extremely slowly in Zn-fa-datz (1) (Supplementary Fig. 4), 195 K CO_2 adsorption isotherm was conducted for the study of the porosity. As we expected, Zn-fa-datz (1) features stronger affinity for C_2H_2 (34.7 kJ mol^{-1}) and C_2H_6 (39.4 kJ mol^{-1}) than C_2H_4 (33.6 kJ mol^{-1}) at the low loading (Fig. 3d, Supplementary Figs. 6–9 and Supplementary Table 2). The equimolar C_2H_2/C_2H_4/C_2H_6 mixture breakthrough experiment shows that C_2H_4 eluted preferentially with high purity (99.9%) from three gases in the fixed-bed adsorber (Fig. 5a), thus further demonstrating that Zn-fa-datz (1) can achieve one-step purification of C_2H_4 in the ternary C2 hydrocarbon mixture. However, due to the lower CO_2 affinity (24.0 kJ mol^{-1}) than for C_2H_4 (33.6 kJ mol^{-1}) (Fig. 3c, d and Supplementary Table 2), Zn-fa-datz (1) failed to produce C_2H_4 in one-step from the equimolar CO_2/C_2H_2/C_2H_4/C_2H_6 quaternary mixture (Fig. 5b).

Regarding the thermodynamic aspect, the adsorption affinity for C_2H_4 should be the lowest among the four adsorbates in order to achieve one-step purification of C_2H_4 from the CO_2/C_2H_2/C_2H_4/C_2H_6 quaternary mixture[49]. For Zn-fa-datz (1), the narrow cavity ensures that the larger C_2H_6 molecule (kinetic diameter = 4.44 Å) can fully contact the pore surface and achieve a higher interaction than the smaller C_2H_4 (kinetic diameter = 4.16 Å). Nevertheless, it also causes C_2H_4 to bind slightly more strongly to the network than the smaller CO_2 (kinetic diameter = 3.30 Å)[53]. We speculated that by fine tuning the pore structure to achieve a more optimized CO_2 adsorption environment, it is possible to reverse the adsorption affinity of C_2H_4 and CO_2 without affecting the adsorption sequence of C_2H_2/C_2H_4/C_2H_6. After carefully analyzing the Zn-fa-datz (1) network, it can be observed that the pore wall of 1D channel is constituted by fa^{2-} ligands and both two amino groups of $datz^-$ ligands through four tight hydrogen-bonding interactions (O-H···N = 1.95–2.12 Å, ∠O-H···N = 138.8–170.4°) (Fig. 2d and Supplementary Fig. 12). The hydrogen bonds restrict the swing of ligands and determine the arrangement of adsorption sites and size/shape of the channel. Hence, we predict that precise pore structure control could be achieved by regulating the hydrogen bonds via different amino side groups (i.e., replacing the diamino $datz^-$ with unilateral-amino 3-amino-1,2,4-triazolate, atz^-).

Synthesis and characterization of Zn-fa-atz (2)

Solvothermal reaction of $Zn(NO_3)_2{\cdot}6H_2O$ with H_2fa and Hatz in a DMF/MeOH/water mixed solvent gave a pillared-layer coordination network with 1D channels, $[Zn_2(fa)(atz)_2]$ (Zn-fa-atz (2)) (Fig. 2b). Single-crystal structure analysis at 298 K revealed that Zn-fa-atz (2) crystallizes in the orthorhombic *Pbca* space group (Supplementary Table 3), isoreticular with previous Zn-fa-datz (1). Both Zn^{2+} ions in Zn-fa-atz (2) exhibit tetrahedral coordination. Each Zn^{2+} ion is coordinated with three N atoms from three atz^-, and one O atom from fa^{2-} (Supplementary Fig. 13). Similar to Zn-fa-datz (1), Zn-fa-atz (2) also exhibits **pcu** topology, which is constructed by the Zn-atz layer based on the dinuclear $[Zn_2(atz)_2]$ unit and the fa^{2-} pillar, but there is an obvious slip between the pillar and the layer (Supplementary Figs. 1–2). The porosity of

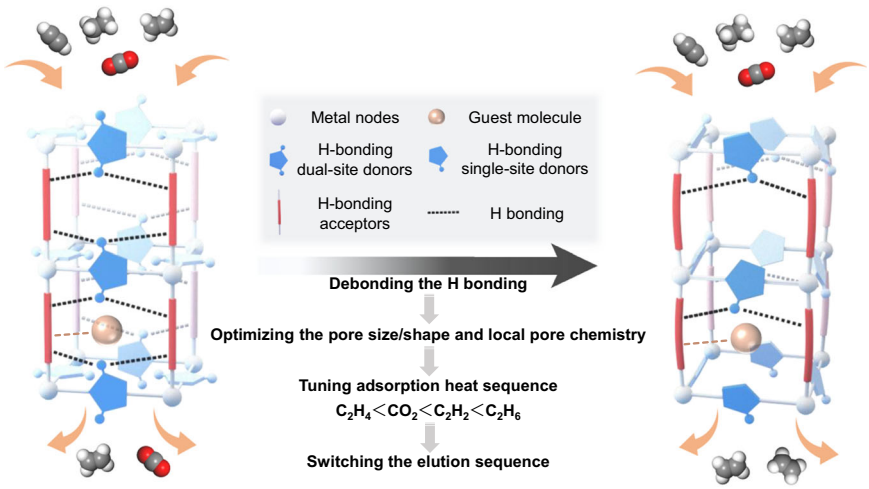

Fig. 1 | Illustration of strategy. Illustration of hydrogen bond unlocking-driven pore size/shape and chemistry control to shift multi-component separation (Color code: metal nodes, white; guest molecule, orange; H-bonding single-site/dual-site donors, blue; H-bonding acceptors, red; H bonding, black dotted line; weak interaction, orange dotted line; the direction of gas flow, orange row; derivation of structure-function relationship, black row).

https://doi.org/10.1038/s41467-024-45081-w

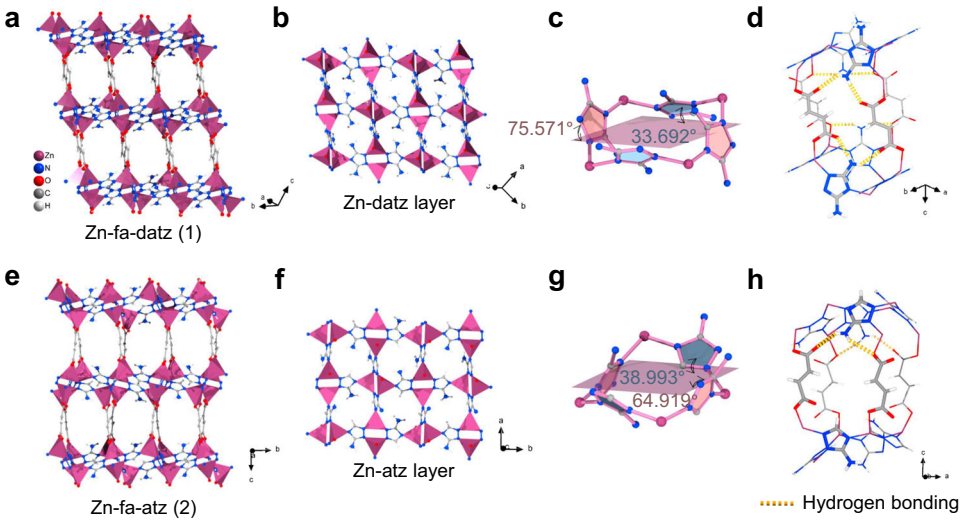

Fig. 2 | Crystal structures. Perspective view of the structure along the 1D channels of Zn-fa-datz (1) (**a**) and Zn-fa-atz (2) (**e**). Zinc–aminotriazolate layer of Zn-fa-datz (1) (**b**) and Zn-fa-atz (2) (**f**). Dihedral angles in Zn-fa-datz (1) (**c**) and Zn-fa-atz (2) (**g**) between atz^-/$datz^-$ and Zn-atz/datz layers. Front views of pore walls with highlighted (yellow) H–N···O interactions of Zn-fa-datz (1) (**d**) and Zn-fa-atz (2) (**h**). Color code: Zn, purple; C, gray; O, red; N, blue; H, white.

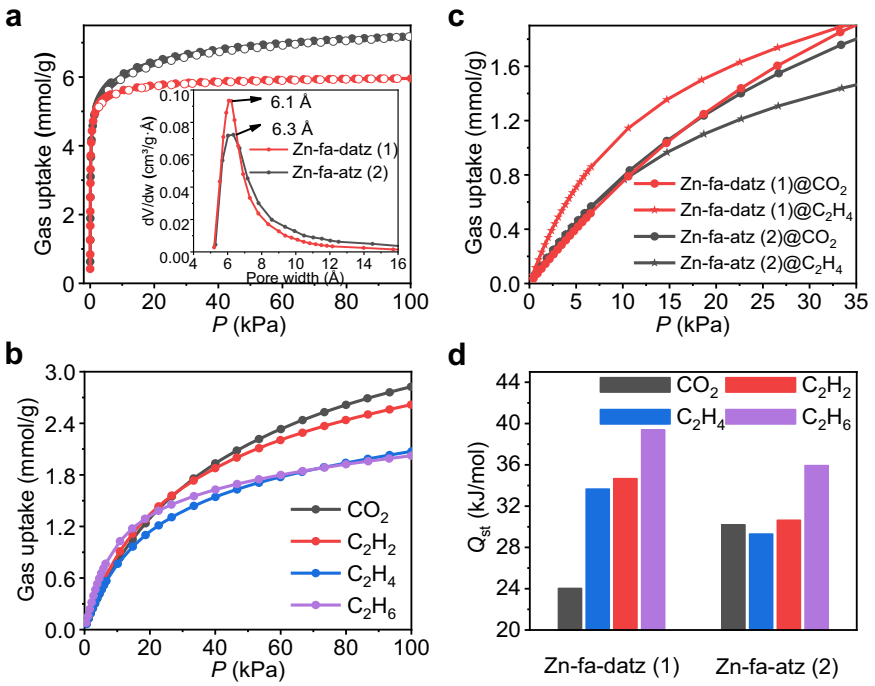

Fig. 3 | Gas adsorption properties of Zn-fa-datz (1) and Zn-fa-atz (2). a CO_2 adsorption isotherms at 195 K (solid: adsorption; open: desorption) and corresponding pore size distributions calculated based on the CO_2 isotherm at 195 K according to the Horvath-Kawazoe model (pore geometry: cylinder) (insert) for Zn-fa-datz (1) (red) and Zn-fa-atz (2) (black). **b** Adsorption isotherms of Zn-fa-atz (2) for CO_2 (black), C_2H_2 (red), C_2H_4 (blue) and C_2H_6 (purple) from 0–100 kPa and 298 K. **c** Comparison of CO_2 (point) and C_2H_4 (star) adsorption isotherms of Zn-fa-datz (1) (red) and Zn-fa-atz (2) (black) from 0 to 35 kPa and 298 K. **d** Comparison of adsorption enthalpies (Q_{st}) of four gases in Zn-fa-datz (1) and Zn-fa-atz (2).

Zn-fa-atz (2) was calculated to be 46.3% (by PLATON[54]) which is larger than that of Zn-fa-datz (1) (38.9%) (Supplementary Table 1). Furthermore, due to the reduction of amino groups, there are fewer hydrogen bonds on the pore walls than Zn-fa-datz (1). For Zn-fa-atz (2), only one side of atz^- ligands are tied to fa^{2-} ligands through two O-H···N hydrogen bonding interactions (O-H···N = 2.12–2.47 Å, ∠O-H···N = 135.6–170.4°) (Fig. 2h and Supplementary Fig. 12). But in Zn-fa-datz (1), both sides of $datz^-$ ligand can connect with fa^{2-} ligands by four hydrogen bonds. When the diagonals between four adjacent O atoms from different fa^{2-} ligands were used to compare the pore sizes of the two structures (minus the van der Waals radius of O atom of 1.52 Å) (Supplementary Fig. 2)[55], it can be seen that the difference in aperture between Zn-fa-atz (2) (5.5 × 4.9 Å) and Zn-fa-datz (1) (5.4 × 4.6 Å) is very small. In fact, debonding the hydrogen bonds causes the rotation of the five-member ring of atz^- ligand, resulting in different dihedral angles between atz^-/$datz^-$ and Zn-atz/datz layers (Fig. 2c, g). Therefore, the greater difference between the Zn-fa-atz (2) and Zn-fa-datz (1) is reflected in the size/shape of the pore and the local pore chemistry.

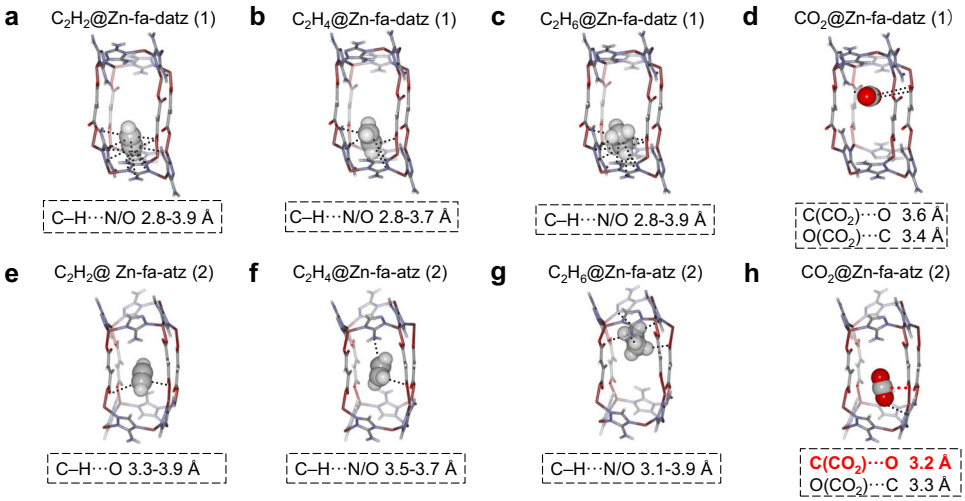

Fig. 4 | The host-guest structures of Zn-fa-datz (1) and Zn-fa-atz (2) revealed by powder diffraction data from Rietveld refinement analysis. a The C_2H_2 binding site, (**b**) C_2H_4 binding site, (**c**) C_2H_6 binding site and (**d**) CO_2 binding site in gas-loaded Zn-fa-datz (1). **e** The C_2H_2 binding site, (**f**) C_2H_4 binding site, (**g**) C_2H_6 binding site and (**h**) CO_2 binding site in gas-loaded Zn-fa-atz (2). Color code: Zn, purple; C, gray; O, red; N, blue; H, white. The graphical representation is created with iRASPA[61].

Thermogravimetry and PXRD data showed that Zn-fa-atz (2) can be fully exchanged with MeOH (Supplementary Figs. 3 and 6). The 195 K CO_2 adsorption isotherm for Zn-fa-atz (2) shows a quasi-type-I characteristic. The pore volume was calculated to be 0.285 $cm^3 g^{-1}$ and 0.283 $cm^3 g^{-1}$ using the CO_2 and N_2 uptake measured at $P/P_0 = 0.96$ and 0.95, respectively, which is comparable with the value calculated from single-crystal diffraction data at 195 K (0.319 $cm^3 g^{-1}$) (Fig. 3a, Supplementary Fig. 14 and Supplementary Table 1). Besides, it is worth to mention that Zn-fa-atz (2) can remain the crystalline and porosity after treated with water or exposed to moisture (*ca.* 35% RH) (Supplementary Fig. 15). The pore size distribution analysis based on the Horvath-Kawazoe model also reveals that the 1D channels of Zn-fa-atz (2) (6.3 Å) comparable with that of Zn-fa-datz (1) (6.1 Å), which is consistent with single-crystal analysis.

Adsorption and separation performances of Zn-fa-atz (2)

Single-component adsorption isotherms for CO_2, C_2H_2, C_2H_4, and C_2H_6 in Zn-fa-atz (2) were measured at 273 K and 298 K (Fig. 3b and Supplementary Fig. 7). At low pressure and 298 K, similar with Zn-fa-datz (1), Zn-fa-atz (2) shows higher uptake for C_2H_6 and C_2H_2 than C_2H_4, indicating the selective adsorption of both adsorbates over C_2H_4. However, the CO_2 uptake for Zn-fa-atz (2) is higher than that for C_2H_4, while the opposite was observed for Zn-fa-datz (1). At 298 K, the adsorption amount sequences of Zn-fa-atz (2) at 14 kPa, 25 kPa and 33 kPa are followed as $C_2H_6 > C_2H_2 > CO_2 > C_2H_4$, $C_2H_2 \approx CO_2 > C_2H_6 > C_2H_4$, and $CO_2 \approx C_2H_2 > C_2H_6 > C_2H_4$, respectively (Supplementary Fig. 16). For Zn-fa-atz (2), the trend in the adsorption enthalpy (Q_{st}) at the low loading is as the following: C_2H_6 (35.9 kJ mol^{-1}) > C_2H_2 (30.6 kJ mol^{-1}) > CO_2 (30.2 kJ mol^{-1}) > C_2H_4 (29.3 kJ mol^{-1}) (Fig. 3d, Supplementary Figs. 7–9 and Supplementary Table 2), while the Q_{st} order of Zn-fa-datz (1) is following as C_2H_6 (39.4 kJ mol^{-1}) > C_2H_2 (34.7 kJ mol^{-1}) > C_2H_4 (33.6 kJ mol^{-1}) > CO_2 (24.0 kJ mol^{-1}). Interestingly, when compared with Zn-fa-datz (1), the $C_2H_2/C_2H_4/C_2H_6$ Q_{st} for Zn-fa-atz (2) decreased synchronously and maintained the same sequence, while the CO_2 Q_{st} showed a significant increase—that is, Zn-fa-atz (2) reversed the C_2H_4/CO_2 adsorption selectivity (Fig. 3c, Supplementary Figs. 10–11 and Supplementary Table 2). Although each of the ideal adsorbed solution theory (IAST) selectivity of the three gases to C_2H_4 are not very high ($CO_2/C_2H_4 = 1.4$, $C_2H_2/C_2H_4 = 1.5$, $C_2H_6/C_2H_4 = 1.4$) (Supplementary Table 2), it is rare to achieve the preferential adsorption of $CO_2/C_2H_2/C_2H_6$ over C_2H_4 at the same time, especially for components with the very close physicochemical properties. The IAST selectivities of Zn-fa-datz (1) and Zn-fa-atz (2) were compared with the best-performing sorbents in the $C_2H_2/C_2H_4/C_2H_6$ three-component system, and $C_2H_2/C_2H_4/C_2H_6/CO_2$ four-component system (Supplementary Table 4). Both Zn-fa-datz (1) and Zn-fa-atz (2) show moderate selectivity for C_2H_2/C_2H_4, C_2H_6/C_2H_4 and CO_2/C_2H_4. In fact, it is very difficult to maintain the lowest selectivity for C_2H_4 among the four gas components, because the physicochemical properties of the four gases are too similar. In general, for ultramicropores without specific binding sites (e.g., open-metal sites), the adsorption affinity mainly comes from the combination of various weak interactions (e.g., van der Waals forces and hydrogen bonding) between the guest molecule and the network in multiple orientations. Consequently, even a slight change in the pore size/shape and local pore chemistry can significantly affect the affinity. In case of Zn-fa-datz (1) and Zn-fa-atz (2), based on the SCXRD analysis, different amino groups not only change the local chemical environment of the pore, but also affect hydrogen bonds in the framework which further leads to the change in the size/shape of the channel (the spatial arrangement of the adsorption sites) (Fig. 2 and Supplementary Figs. 2 and 12).

Host-guest structure studies

To further understand the role of pore structure tuning, the host–guest structures of Zn-fa-datz (1) and Zn-fa-atz (2) were studied by the PXRD analyses and corresponding refinements (Fig. 4, Supplementary Figs. 17–20 and Supplementary Table 5). The eight studied hos–guest systems showed that all the gas molecules preferentially localized within the pockets enclosed by four triazolate moieties and four fa^{2-} ligands. For $C_2H_2/C_2H_4/C_2H_6$, the host–guest interactions are mainly contributed by weak O/N···H–C hydrogen bonding interactions from multiple orientations. C_2H_2, C_2H_4, and C_2H_6 are all confined in the relatively spacious positions in the cavities of Zn-fa-datz (1) and Zn-fa-atz (2), but the molecular orientations change due to the difference in pore shape and pore chemistry. As shown in Fig. 4 and Supplementary Table 5, most measured O/N···H–C distances in Zn-fa-atz (2) are slightly longer than that in Zn-fa-datz (1), which is consistent with the synchronous decrease of the Q_{st} for the three C2 hydrocarbons in Zn-fa-atz (2). For CO_2 in Zn-fa-atz (2) (Fig. 4), the optimal position has changed when compared with that in Zn-fa-datz (1), and the O atom from the framework can contact closely with the C atom in CO_2, yielding a relative strong

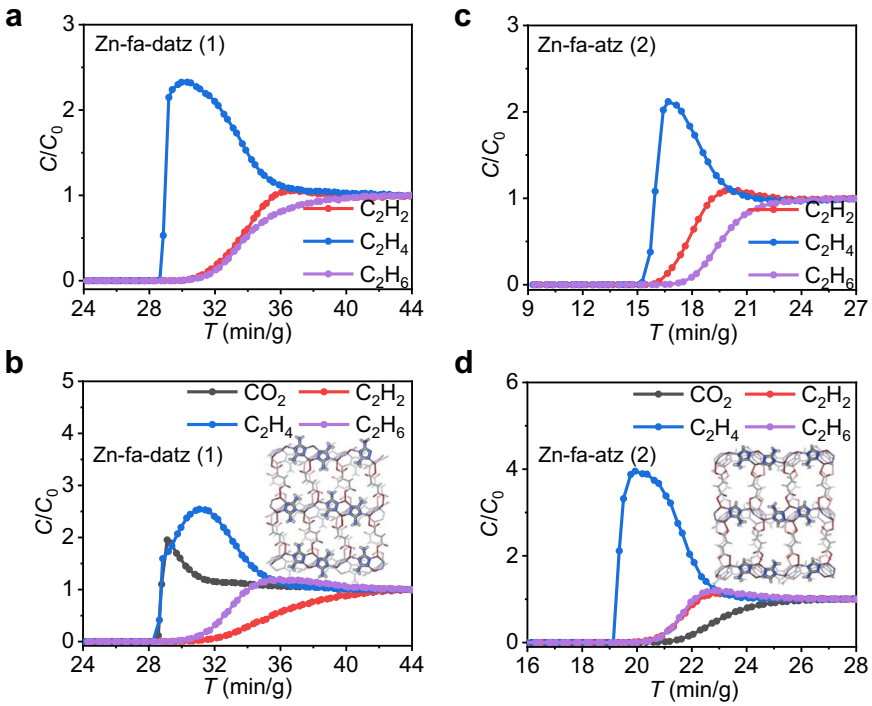

Fig. 5 | Experimental breakthrough experiments. Experimental column breakthrough curves at 298 K for: Zn-fa-datz (1) powder using a mixture of (**a**) $C_2H_2/C_2H_4/C_2H_6$/He (1:1:1:4, total gas pressure of 1 bar, total flowing rate of 3.5 mL/min), and an equimolar mixture of (**b**) $CO_2/C_2H_2/C_2H_4/C_2H_6$ (1:1:1:1, total gas pressure of 1 bar, total flowing rate of 2 mL/min). Zn-fa-atz (2) powder using (**c**) $C_2H_2/C_2H_4/C_2H_6$/He (1:1:1:4) and (**d**) $CO_2/C_2H_2/C_2H_4/C_2H_6$ (1:1:1:1). Color code: Zn, purple; C, gray; O, red; N, blue; H, white.

interaction (C···O = 3.231 Å) that cannot be observed in Zn-fa-datz (1), resulting in higher CO_2 Q_{st} than that of Zn-fa-datz (1).

Dynamic breakthrough experiments of Zn-fa-atz (2) and Zn-fa-atz (2)/PES composite beads

To evaluate the gas separation performance, breakthrough experiments were performed with Zn-fa-atz (2). At 298 K and ambient pressure, $C_2H_2/C_2H_4/C_2H_6$/He and equimolar $CO_2/C_2H_2/C_2H_4/C_2H_6$ mixtures were passed through the column packed with Zn-fa-atz (2) powder (Fig. 5). The outlet gases were monitored by the online gas chromatography. As shown in Fig. 5c, d, C_2H_4 breaks through first from the column at 15 min g^{-1} and 19 min g^{-1}, respectively, which is consistent with the adsorption isotherms. Before the impurities flowed out, the purity of C_2H_4 at the outlet reached that of polymer grade (>99.9%) (Supplementary Fig. 21), demonstrating that Zn-fa-atz (2) achieved the one-step purification of C_2H_4 from both the $C_2H_2/C_2H_4/C_2H_6$/He and $CO_2/C_2H_2/C_2H_4/C_2H_6$ mixtures. It is worth mentioning that the different gas elution orders of three- and four-component separation are related to the order of adsorption capacity of each gas at different partial pressures (Supplementary Table 6). In contrast, Zn-fa-datz (1) can only realize one-step C_2H_4 production from ternary $C_2H_2/C_2H_4/C_2H_6$ mixture. To test the recycling performance of Zn-fa-atz (2), three cycles of breakthrough and following desorption experiments were conducted (Supplementary Figs. 22–23). There was no significant change in the C_2H_4 retention time and the separation performance, revealing the favorable recyclability and facile regeneration of Zn-fa-atz (2). Moreover, the highly consistent breakthrough data from three different batches of samples also fully verified the reproducibility of the samples and experiments (Supplementary Fig. 24). The simulated breakthrough curves were conducted to further validate the feasibility of Zn-fa-atz (2) for the separation performance (Supplementary Fig. 25), which is highly consistent with our experimental results. However, when Zn-fa-atz (2) was exposed to wet quaternary mixtures (*ca.* 36% RH), the breakthrough curves showed that Zn-fa-atz (2) can maintain the elution sequence, but the retention times and the shape of the breakthrough curves have changed significantly, indicating the competitive adsorption of water with the other four gases (Supplementary Fig. 26).

To verify the competitive adsorption during the breakthrough experiments, we calculated the actual uptakes of Zn-fa-datz (1) and Zn-fa-atz (2) for the four gases using the reported method (Supplementary Figs. 27–28 and Supplementary Tables 7–8)[56–58]. The results show that the actual selectivities are little different from that of IAST selectivities. For Zn-fa-atz (2), the adsorption amount order of each gas is followed as $CO_2 > C_2H_2 > C_2H_6 > C_2H_4$, being similar with the isotherms, but the selectivity changed in CO_2/C_2H_4 ($S_{breakthrough} = 2.17 > S_{IAST} = 1.4$). For Zn-fa-datz (1), the adsorption amount order for each gas is followed as $C_2H_2 > C_2H_6 > CO_2 > C_2H_4$, which is inconsistent with that of the isotherms ($C_2H_2 > C_2H_6 > C_2H_4 > CO_2$), and the selectivity of CO_2/C_2H_4 also changed ($S_{breakthrough} = 1.27 > S_{IAST} = 0.8$). Obviously, both Zn-fa-atz (2) and Zn-fa-datz (1) have different degrees of increase in the adsorption of CO_2 in the breakthrough experiments. Therefore, the diffusion coefficients of the four gases through the adsorption kinetic profiles at 298 K (Supplementary Fig. 29) were calculated. The results showed that the diffusion of CO_2 (0.3874) was significantly higher than that of C_2H_4 (0.1191), C_2H_2 (0.0820), and C_2H_6 (0.0478), indicating CO_2 diffused much faster than other three gases during the breakthrough experiments. Therefore, the larger uptakes of CO_2 are the result of the synergistic effect of adsorption thermodynamics and kinetics.

In addition, for practical industrial applications, the Zn-fa-atz (2) crystals were shaped into spherical pellets, with addition of organic polymer binder. In presence of 20 wt% of poly-ether sulfone (PES) as the binder, the Zn-fa-atz (2)/PES composite beads with a diameter of *ca.* 2.5 mm were successfully fabricated via the phase inversion method (Supplementary Fig. 30). The scanning electron microscope (SEM) images show Zn-fa-atz (2) crystals (*ca.* 500 nm) are well embedded within the inner polymer matrix (Supplementary Fig. 30b, c). The CO_2 adsorption isotherm at 195 K of Zn-fa-atz (2)/PES also

shows a quasi-type-I characteristic, indicating the microporosity of the beads (Supplementary Figs. 30d, e and 31). The pore volume was calculated to be 0.265 $cm^3 g^{-1}$ at $P/P_0 = 0.96$ (7% lower than that of pure Zn-fa-atz (2) crystal sample), suggesting that Zn-fa-atz (2)/PES retains most of the porosity. Further, the kinetic adsorption profiles for C_2H_6 were measured at 298 K and 1 atm. The diffusional rate constants (k)[59] for C_2H_6 in Zn-fa-atz (2)/PES was calculated to be 1.1437, which is within the vicinity of that for the Zn-fa-atz (2) powder ($k = 1.2706$), meaning that compositing has little effect on the gas diffusion (Supplementary Fig. 32). The equimolar $CO_2/C_2H_2/C_2H_4/C_2H_6$ mixture breakthrough experiment was further tested with Zn-fa-atz (2)/PES beads-packed column at room temperature. As shown in Supplementary Fig. 30f, C_2H_4 breakthrough first at 18 min g^{-1}, following by C_2H_6, CO_2, and C_2H_2, indicating the effective one-step C_2H_4 production ability from quaternary mixture after shaping Zn-fa-atz (2) into PES-based spherical pellets.

Discussion

In conclusion, fine-tuning pore size/shape and local pore chemistry by regulating the network hydrogen bonding interactions in two related coordination networks can precisely control the adsorption selectivity of C_2H_4 in the complex separation systems. The reported ultramicroporous adsorbent, Zn-fa-atz (2), can achieve the effective one-step purification of C_2H_4 from $CO_2/C_2H_2/C_2H_4/C_2H_6$ quaternary mixture. Design principle presented here could be helpful to advance the new-generation physisorbent synthesis and application for more complex industry-related separation system.

Methods

Synthesis of Zn-fa-datz (1)

According to the reported procedures with a little modification[52]. $Zn(NO_3)_2.6H_2O$ (1.0 mmol, 0.298 g), fumaric acid (H_2fa, 0.5 mmol, 0.058 g), 1*H*-1,2,4-triazole-3,5-diamino (Hdatz, 1.0 mmol, 0.099 g) were dissolved in 10 mL DMF/MeOH/H_2O mixed solution (4:4:2, $v/v/v$). After 30 min of sonication treatment, the resulting solution was sealed in a 25 mL Teflon-lined stainless-steel autoclave and heated at 130 °C under autogenous pressure for 72 h. After slowly cooling down to room temperature, the colorless crystals of Zn-fa-datz (1) were washed with DMF/MeOH (1:1, v/v) mixed solution for three times, and dried at room temperature (yield = 48% based on Zn). The obtained sample was exchanged with fresh MeOH three times daily for three days.

Synthesis of Zn-fa-atz (2)

$Zn(NO_3)_2{\cdot}6H_2O$ (1.0 mmol, 0.298 g), fumaric acid (H_2fa, 0.5 mmol, 0.058 g), 3-amino-1,2,4-triazole (Hatz, 1.0 mmol, 0.084 g) were dissolved in 10 mL DMF/MeOH/H_2O mixed solution (4:4:2, $v/v/v$). After 30 min of sonication, the resulting solution was sealed in a 25 mL Teflon-lined stainless-steel autoclave and heated at 130 °C under autogenous pressure for 72 h. After slowly cooling down to room temperature, the colourless crystals of Zn-fa-atz (2) were washed with fresh DMF/MeOH (1:1, v/v) mixed solution for three times, and dried at room temperature (yield = 52% based on Zn). The obtained sample was exchanged with fresh MeOH three times daily for three days.

Gas adsorption measurements

The thermodynamic adsorption isotherms for CO_2, C_2H_2, C_2H_4, and C_2H_6 were conducted on 3FLEX (Micromertics). Before the N_2 (77 K)/CO_2 (195 K) adsorption measurement, Zn-fa-atz (2) powder, Zn-fa-datz (1) powder and Zn-fa-atz (2)/PES beads (~100 mg) were evacuated under a dynamic vacuum at 75 °C for 4 h to remove the guest molecules.

Dynamic breakthrough experiments

Before breakthrough experiments, the samples were packed in a column and activated in-situ by heating at 75 °C for 20 h in a He flow with rate of 20 mL/min, and then cooled to room temperature. Then the gas flow is switched to the desired gas mixture (v(He)/v(C_2H_2)/v(C_2H_4)/v(C_2H_6) = 58:14:14:14, v(CO_2)/v(C_2H_2)/v(C_2H_4)/v(C_2H_6) = 25:25:25:25). The dynamic breakthrough data were recorded on a homemade apparatus at room temperature and 1 atm. The gas stream concentration at column outlet was continuously detected by using a chromatographic analyzer (TCD-Thermal Conductivity Detector, detection limit 0.1 ppm). After equilibrium, desorption curves of Zn-fa-atz (2) in Supplementary Fig. 23 was collected under a He flow of 20 mL/min at 70 °C.

Reporting summary

Further information on research design is available in the Nature Portfolio Reporting Summary linked to this article.

Data availability

For full characterization data including detailed sorption and breakthrough experiments data see the Supplementary Methods 3 and 5. All data supporting the finding of this study are available within this article and its Supplementary Information. Crystallographic data for Zn-fa-atz (2) reported in this article have been deposited at the Cambridge Crystallographic Data Centre, under deposition numbers CCDC 2176255-2176256. Copies of the data can be obtained free of charge via https://www.ccdc.cam.ac.uk/structures/. Source data of the PXRD patterns, TGA curves, sorption tests; gas adsorption enthalpies and selectivities, Rietveld refinement of powder X-ray diffraction tests and breakthrough tests that support the findings of this study are provided as a Source Data file (ref. 60. Rong, Y. (2023): Source data of Zn-fa-datz (1) and Zn-fa-atz (2) that support the findings of this study.xlsx. Data sets. figshare https://doi.org/10.6084/m9.figshare.24864540). Source data are provided with this paper.

References

1. Yang, Y. et al. Ethylene/ethane separation in a stable hydrogen-bonded organic framework through a gating mechanism. *Nat. Chem.* **13**, 933–939 (2021).
2. Chen, K. et al. Synergistic sorbent separation for one-step ethylene purification from a four-component mixture. *Science* **366**, 241–246 (2019).
3. Bao, Z. et al. Potential of microporous metal–organic frameworks for separation of hydrocarbon mixtures. *Energy Environ. Sci.* **9**, 3612–3641 (2016).
4. Ren, T., Patel, M. & Blok, K. Olefins from conventional and heavy feedstocks: energy use in steam cracking and alternative processes. *Energy* **31**, 425–451 (2006).
5. Angelini, P. et al. *Materials for Separation Technologies: Energy and Emission Reduction Opportunities*. (Oak Ridge National Lab. (ORNL), Oak Ridge, TN (United States), 2005).
6. Li, J., Kuppler, R. J. & Zhou, H. Selective gas adsorption and separation in metal–organic frameworks. *Chem. Soc. Rev.* **38**, 1477–1504 (2009).
7. Zhou, H. & Kitagawa, S. Metal-organic frameworks (MOFs). *Chem. Soc. Rev.* **43**, 5415–5418 (2014).
8. Li, H. et al. Porous metal-organic frameworks for gas storage and separation: Status and challenges. *EnergyChem* **1**, 100006 (2019).
9. Zhou, D. et al. Adsorptive separation of carbon dioxide: from conventional porous materials to metal–organic frameworks. *EnergyChem* **1**, 100016 (2019).
10. Wang, H., Liu, Y. & Li, J. Designer metal–organic frameworks for size-exclusion-based hydrocarbon separations: progress and challenges. *Adv. Mater.* **32**, 2002603 (2020).
11. Kitagawa, S., Kitaura, R. & Noro, S. I. Functional porous coordination polymers. *Angew. Chem. Int. Ed.* **43**, 2334–2375 (2004).
12. Perry, J. J. IV, Perman, J. A. & Zaworotko, M. J. Design and synthesis of metal–organic frameworks using metal–organic polyhedra as

supermolecular building blocks. *Chem. Soc. Rev.* **38**, 1400–1417 (2009).
13. Krause, S. et al. A pressure-amplifying framework material with negative gas adsorption transitions. *Nature* **532**, 348–352 (2016).
14. Zhou, D. & Zhang, J. On the role of flexibility for adsorptive separation. *Acc. Chem. Res.* **55**, 2966–2977 (2022).
15. Zhou, M., El-Sayed, E. S. M., Ju, Z., Wang, W. & Yuan, D. The synthesis and applications of chiral pyrrolidine functionalized metal–organic frameworks and covalent-organic frameworks. *Inorg. Chem. Front.* **7**, 1319–1333 (2020).
16. Cui, X. et al. Pore chemistry and size control in hybrid porous materials for acetylene capture from ethylene. *Science* **353**, 141–144 (2016).
17. Li, B. et al. An ideal molecular sieve for acetylene removal from ethylene with record selectivity and productivity. *Adv. Mater.* **29**, 1704210 (2017).
18. Zhang, Y. et al. Rational design of microporous MOFs with anionic boron cluster functionality and cooperative dihydrogen binding sites for highly selective capture of acetylene. *Angew. Chem. Int. Ed.* **59**, 17664–17669 (2020).
19. Zhang, Z. et al. Efficient trapping of trace acetylene from ethylene in an ultramicroporous metal–organic framework: synergistic effect of high-density open metal and electronegative sites. *Angew. Chem. Int. Ed.* **59**, 18927–18932 (2020).
20. Dong, Q. et al. Shape- and size-dependent kinetic ethylene sieving from a ternary mixture by a trap-and-flow channel crystal. *Adv. Funct. Mater.* **32**, 2203745 (2022).
21. Xue, Y. et al. Precise pore space partitions combined with high-density hydrogen-bonding acceptors within metal–organic frameworks for highly efficient acetylene storage and separation. *Angew. Chem. Int. Ed.* **60**, 10122–10128 (2021).
22. Wang, J. et al. De-linker-enabled exceptional volumetric acetylene storage capacity and benchmark C_2H_2/C_2H_4 and C_2H_2/CO_2 separations in metal-organic frameworks. *Angew. Chem. Int. Ed.* https://doi.org/10.1002/anie.202217839 (2023).
23. Shen, J. et al. Simultaneous interlayer and intralayer space control in two-dimensional metal–organic frameworks for acetylene/ethylene separation. *Nat. Commun.* **11**, 6259 (2020).
24. Bloch, E. D. et al. Hydrocarbon separations in a metal-organic framework with open iron (II) coordination sites. *Science* **335**, 1606–1610 (2012).
25. Liao, P., Zhang, W., Zhang, J. & Chen, X. Efficient purification of ethene by an ethane-trapping metal-organic framework. *Nat. Commun.* **6**, 8697 (2015).
26. Li, L. et al. Ethane/ethylene separation in a metal-organic framework with iron-peroxo sites. *Science* **362**, 443–446 (2018).
27. Lin, R. et al. Molecular sieving of ethylene from ethane using a rigid metal–organic framework. *Nat. Mater.* **17**, 1128–1133 (2018).
28. Gu, C. et al. Design and control of gas diffusion process in a nanoporous soft crystal. *Science* **363**, 387–391 (2019).
29. Li, Y. et al. Ultrahigh-uptake capacity-enabled gas separation and fruit preservation by a new single-walled nickel–organic framework. *Adv. Sci.* **8**, 2003141 (2021).
30. Wang, G. et al. Boosting ethane/ethylene separation by mofs through the amino-functionalization of pores. *Angew. Chem. Int. Ed.* **61**, e202213015 (2022).
31. Geng, S. et al. Scalable room-temperature synthesis of highly robust ethane-selective metal–organic Frameworks for Efficient Ethylene Purification. *J. Am. Chem. Soc.* **143**, 8654–8660 (2021).
32. Zhang, J. & Chen, X. Optimized acetylene/carbon dioxide sorption in a dynamic porous crystal. *J. Am. Chem. Soc.* **131**, 5516–5521 (2009).
33. Zhang, L. et al. Benchmark C_2H_2/CO_2 separation in an ultramicroporous metal-organic framework via Copper(I)-alkynyl chemistry. *Angew. Chem. Int. Ed.* **60**, 15995–16002 (2021).
34. Li, H. et al. An unprecedented pillar-cage fluorinated hybrid porous framework with highly efficient acetylene storage and separation. *Angew. Chem. Int. Ed.* **60**, 7547–7552 (2021).
35. Di, Z. et al. Cage-like porous materials with simultaneous high C_2H_2 storage and excellent C_2H_2/CO_2 separation performance. *Angew. Chem. Int. Ed.* **60**, 10828–10832 (2021).
36. Yang, L. et al. Adsorption site selective occupation strategy within a metal–organic framework for highly efficient sieving acetylene from carbon dioxide. *Angew. Chem. Int. Ed.* **133**, 4620–4624 (2021).
37. Reid, C. R. & Thomas, K. M. Adsorption kinetics and size exclusion properties of probe molecules for the selective porosity in a carbon molecular sieve used for air separation. *J. Phys. Chem. B* **105**, 10619–10629 (2001).
38. Sircar, S. Basic research needs for design of adsorptive gas separation processes. *Ind. Eng. Chem. Res.* **45**, 5435–5448 (2006).
39. Eguchi, R., Uchida, S. & Mizuno, N. Inverse and High CO_2/C_2H_2 sorption selectivity in flexible organic–inorganic ionic crystals. *Angew. Chem. Int. Ed.* **51**, 1635–1639 (2012).
40. Hao, H. et al. Simultaneous trapping of C_2H_2 and C_2H_6 from a ternary mixture of $C_2H_2/C_2H_4/C_2H_6$ in a robust metal-organic framework for the purification of C_2H_4. *Angew. Chem. Int. Ed.* **130**, 16299–16303 (2018).
41. Wang, Y. et al. One-step ethylene purification from an acetylene/ethylene/ethane ternary mixture by cyclopentadiene cobalt-functionalized metal-organic frameworks. *Angew. Chem. Int. Ed.* **60**, 11350–11358 (2021).
42. Wang, G. et al. One-step C_2H_4 purification from ternary $C_2H_6/C_2H_4/C_2H_2$ mixtures by a robust metal-organic framework with customized pore environment. *Angew. Chem. Int. Ed.* **61**, https://doi.org/10.1002/anie.202205427 (2022).
43. Gu, X. et al. Immobilization of lewis basic sites into a stable ethane-selective MOF enabling one-step separation of ethylene from a ternary mixture. *J. Am. Chem. Soc.* **144**, 2614–2623 (2022).
44. Yang, S. et al. Efficient purification of ethylene from C2 hydrocarbons with an C_2H_6/C_2H_2-selective metal-organic framework. *ACS Appl. Mater. Interfaces* **13**, 962–969 (2021).
45. Jiang, Z. et al. An aromatic-rich cage-based MOF with inorganic chloride ions decorating the pore surface displaying the preferential adsorption of C2H2 and C2H6 over C2H4. *Inorg. Chem. Front.* **8**, 1243–1252 (2021).
46. Fan, L. et al. Rational construction and performance regulation of an In(III)–tetraisophthalate framework for one-step adsorption-phase purification of C_2H_4 from C_2 hydrocarbons. *Inorg. Chem.* **60**, 10819–10829 (2021).
47. Xu, Z. et al. A robust Th-azole framework for highly efficient purification of C_2H_4 from a $C_2H_4/C_2H_2/C_2H_6$ mixture. *Nat. Commun.* **11**, 3163 (2020).
48. Zhang, P. et al. Synergistic binding sites in a hybrid ultramicroporous material for one-step ethylene purification from ternary C(2) hydrocarbon mixtures. *Sci. Adv.* **8**, https://doi.org/10.1126/sciadv.abn9231 (2022)
49. Cao, J. et al. One-step ethylene production from a four-component gas mixture by a single physisorbent. *Nat. Commun.* **12**, 6507 (2021).
50. Laha, S. et al. Tailoring Robust Al-MOF for Trapping C_2H_6 and C_2H_2 towards Efficient C_2H_4 purification from quaternary mixtures. *Chem. Sci.* **13**, 7172–7180 (2022).
51. Zhang, T. et al. General pore features for one-step C_2H_4 production from a C2 hydrocarbon mixture. *Chem. Commun.* **58**, 4954–4957 (2022).
52. Xing, G., Liu, Q., Zhang, Y., Zhang, S. & Dong, Y. Microporous Zinc (II) metal-organic framework with 6-Connected pcu topology: synthesis, structure, and gas adsorption properties. *Z. Anorg. Allg. Chem.* **641**, 1556–1559 (2015).

53. Mukherjee, S., Sensharma, D., Chen, K. & Zaworotko, M. Crystal engineering of porous coordination networks to enable separation of C2 hydrocarbons. *Chem. Commun.* **56**, 10419–10441 (2020).
54. Spek, A. L. Single-crystal structure validation with the program PLATON. *J. Appl. Crystallogr.* **36**, 7–13 (2003).
55. Bondi, A. Van der Waals volumes and radii. *J. Phys. Chem.* **68**, 441–451 (1964).
56. Wang, Y. et al. Selective aerobic oxidation of a metal-organic framework boosts thermodynamic and kinetic propylene/propane selectivity. *Angew. Chem. Int. Ed.* **58**, 7692–7696 (2019).
57. Zhang, X. W. et al. Tuning the gating energy barrier of metal-organic framework for molecular sieving. *Chem* **7**, 1006–1019 (2021).
58. Ye, Z. M. et al. A hydrogen-bonded yet hydrophobic porous molecular crystal for molecular-sieving-like separation of butane and isobutane. *Angew. Chem. Int. Ed.* **59**, 23322–23328 (2020).
59. Fletcher, A. J. et al. Adsorption dynamics of gases and vapors on the nanoporous metal organic framework material Ni_2(4,4′-bipyridine)$_3$(NO_3)$_4$: guest modification of host sorption behavior. *J. Am. Chem. Soc.* **123**, 10001–10011 (2001).
60. Yang, R. et al. Source data of Zn-fa-datz (1) and Zn-fa-atz (2) that support the findings of this study. Data sets. figshare https://doi.org/10.6084/m9.figshare.24864540 (2023).
61. Dubbeldam, D., Calero, S. & Vlugt, T. J. iRASPA: GPU-accelerated visualization software for materials scientists. *Mol. Simulat.* **44**, 653–676 (2018).

Acknowledgements

We appreciate the financial support from the National Natural Science Foundation of China (22071195, K.-J. C., 22101231, Y.W.), the Youth Innovation Team of Shaanxi Universities and China Postdoctoral Science Foundation (No. 2022M712585, T.Z.). We are also thankful for the help from Prof. Dr. Bao-Yong Zhu, Prof. Dr. Hui Wang and Mr. You Wang. T.P. and K.A.F. acknowledge the use of services provided by Research Computing at the University of South Florida.

Author contributions

K.-J.C. designed the project. R.Y., Y.W., J-W.C., T.G., X.-O.X. and Q.-H.Y. synthesized the compounds, J.-W.C., X.J., R.Y., Y.W. and T.G. collected all adsorption data. T.P. and K.A.F. participated in the separation mechanism discussion. R.Y., Y.W. and J-W.C. collected the experimental breakthrough data. R.K. carried out the breakthrough simulation. H.C. and L.Li participated in the breakthrough simulation discussion. Y.W. and T.G. collected the SEM data. R.Y. and Y.W. analyzed the adsorption data and experimental breakthrough data. Y.W., B.-K.L. and T.Z. analyzed the single crystal data, Y.W. and Z.-M.Y. collected and analyzed the powder refinement data. Y.W., R.Y. and K.-J.C. wrote the paper, and all authors contributed to revise the manuscript.

Competing interests

The authors declare no competing interests.

Additional information

Supplementary information The online version contains supplementary material available at https://doi.org/10.1038/s41467-024-45081-w.

Correspondence and requests for materials should be addressed to Kai-Jie Chen.

Peer review information *Nature Communications* thanks Ho Bum Park, and the other, anonymous, reviewer(s) for their contribution to the peer review of this work. A peer review file is available.

Supplementary Information

Hydrogen Bond Unlocking-Driven Pore Structure Control for Shifting Multi-Component Gas Separation Function

Rong Yang,[1, †] Yu Wang,[1, †] Jian-Wei Cao,[1] Zi-Ming Ye,[2] Tony Pham,[3] Katherine A. Forrest,[3] Rajamani Krishna,[4] Hongwei Chen,[5] Libo Li,[5] Bo-Kai Ling,[1] Tao Zhang,[1] Tong Gao,[1] Xue Jiang,[1] Xiang-Ou Xu,[1] Qian-Hao Ye,[1] & Kai-Jie Chen[1,*]

[1]Key Laboratory of Special Functional and Smart Polymer Materials of Ministry of Industry and Information Technology, Xi'an Key Laboratory of Functional Organic Porous Materials, School of Chemistry and Chemical Engineering, Northwestern Polytechnical University, Xi'an, Shaanxi 710072, P.R. China

[2]Fujian Key Laboratory of Polymer Materials, College of Chemistry and Materials Science, Fujian Normal University, Fuzhou 350007, P.R. China

[3]Department of Chemistry, University of South Florida, 4202 East Fowler Avenue, CHE205, Tampa, Florida 33620-5250, USA

[4]Van 't Hoff Institute for Molecular Sciences, University of Amsterdam, Science Park 904, 1098 XH Amsterdam, The Netherlands.

[5]Shanxi Key Laboratory of Gas Energy Efficient and Clean Utilization, College of Chemical Engineering and Technology, Taiyuan University of Technology, Taiyuan, P.R. China.

*Corresponding authors: ckjiscon@nwpu.edu.cn

[†]R.Y. and Y.W. have contributed equally.

Table of Contents

Supplementary Methods 1. Materials and Synthesis of Zn-fa-atz (2)/PES composite beads

Poly(ether sulfone) powder (PES, E6020, M_W~150000 by GPC, 99%) was purchased from BASF chemical company (Germany). Other materials: zinc nitrate hexahydrate ($Zn(NO_3)_2$.$6H_2O$, 99%), fumaric acid (H_2fa, 99%), 3-amino-1,2,4-triazole (Hatz, 96%), 1*H*-1,2,4-triazole-3,5-diamino (Hdatz, 98%), methanol (MeOH, 99%), N, N-dimethylformamide (DMF, 99%), were purchased and used without further purification.

He (99.999%), N_2 (99.999%), CO_2 (99.995%), C_2H_2 (99.9%), C_2H_4 (99.999%), and C_2H_6 (99.999%) were purchased from Jinan Heli Special Gas Co., Ltd (china).

The Zn-fa-atz (2)/PES beads were prepared via the phase inversion method: typically, 0.2 g of PES was dissolved in 1 mL of DMF. The mixture was stirred until PES was completely dissolved in DMF at room temperature. Then, 0.8 g of Zn-fa-atz (2) was dispersed in the above polymer solution and stirred for another 5 min. The resulting polymer slurry was vertically pipetted to a 100 mL MeOH coagulation bath (stirring on a magnetic stir plate) through a 1 mL fine stainless-steel syringe tip with a size of 21 gauge (0.8 mm in inner diameter). The air gap was about 6 cm, the droplets were slowly added to MeOH and immediately solidified to beads via solvent/MeOH exchange. The loading of Zn-fa-atz (2) in the obtained Zn-fa-atz (2)/PES composite beads is 80 wt% (considering there is no weight loss during the phase inversion method). Finally, the beads were transferred to 250 mL scintillation vial glass bottles filled with fresh MeOH and exchanged with fresh MeOH three times daily for three days.

Supplementary Methods 2. Physical Measurements

Powder X-ray diffraction (PXRD) patterns were recorded on a Rigaku Mini Flex II X-ray diffractometer (Cu K_α, λ = 1.54059 Å) with an operating power of 40 kV, 15 mA. All samples were subjected to scanning at 2θ from 5–50° with a scanning rate of 5 °/min. Thermogravimetric analyses (TGA) were conducted by using a METTLER TGA2 instrument in N_2 flow with a heating rate of 10 °C/min from 30 to 800 °C. Scanning Electron Microscopy (SEM) images were collected using the FEI Verios G4 SEM instrument at an acceleration voltage of 5–20 kV to investigate the surface and the cross-section morphology of Zn-fa-atz (2)/PES composite beads.

Supplementary Methods 3. Kinetic adsorption measurements

Time-dependent adsorption determination of CO_2/C_2H_2/C_2H_4/C_2H_6 was performed with a TA Instruments Discovery thermobalance at 298 K and 1 atm or an automatic volumetric adsorption apparatus BELSORP-HP at 298 K. Prior to each adsorption measurement, the samples were activated at 75 °C for 0.5/4 h under N_2 or a high vacuum. The resulting curves was used to calculate the diffusional time constants by using the following Eq.1 or Eq.2:

$$\frac{M_t}{M_e} = 1 - \exp(-kt) \qquad (1)$$

Where M_t is the mass uptake at time t, M_e is the mass uptake at equilibrium, and k is the kinetic rate constant.[1] After normalization of kinetic adsorption data, t (min) and M_t/M_e were taken as x and y axes, respectively.

$$\frac{M_t}{M_e} = \frac{6}{\sqrt{\pi}} \cdot \sqrt{\frac{D}{r^2}} \cdot \sqrt{t} \qquad (2)$$

Where M_t is the gas adsorbed amount at time t, M_e is the gas adsorbed amount at equilibrium, D is the diffusivity and r is the radius of the equivalent spherical particle.[2]Therefore, the slopes of q_t/q_∞ versus $\sqrt{t}$ are derived from the fitting of the plots in the low gas adsorbed amount range, and then D' is obtained from the square of the slope multiplying by π/36.

Supplementary Methods 4. Single X-ray diffraction characterization

Crystal data of Zn-fa-atz (2) were collected at 195 K and 298 K on a Bruker D8 Venture diffractometer equipped with Ga Kα microfocus X-ray generator (λ=1.34139 Å), Photon II detector. The data were empirically corrected for X-ray adsorption with Sadabs,[3,4] in the

Bruker APEX II software suite. The structures were solved by the direct method and refined with the full-matrix least-squares technique using the SHELXTL program package.[4,5] Anisotropic thermal parameters were applied to all non-hydrogen atoms. Hydrogen atoms were generated geometrically (C–H 0.95 Å). The Olex Solvent Mask treatment was applied because the guest molecule is extremely disordered and cannot be modeled. The crystallographic data of Zn-fa-atz (2) were summarized in Supplementary Table 3, and ORTEP style illustrations of the structure are provided in Supplementary Figure 13. The crystal structure has been deposited at the Cambridge Crystallographic Data Centre (CCDC), under deposition number CCDC 2176255-2176256, and can be obtained free of charge (http://www.ccdc.cam.ac.uk/data_request/cif).

Supplementary Notes 1. Calculation of adsorption enthalpy

$$\ln(P) = \ln(N) + (\frac{1}{T})\sum_{i=0}^{m} a_i N^i + \sum_{j=0}^{n} b_j N^j \qquad (3)$$

In order to extract the coverage-dependent adsorption enthalpy, the isotherm data of Zn-fa-datz (1) and Zn-fa-atz (2) were fitted with a virial-type expression of the above form at 273 K and 298 K, where *P* is the pressure in kPa, *N* is the amount uptake in mmol/g, *T* is the temperature in K, a_i and b_j are virial coefficients that are independent of temperature, and *m* and *n* are the number of coefficients used to adequately describe the isotherm.

$$Q_{st} = -R\sum_{i=0}^{n} a_i N^i \qquad (4)$$

Where Q_{st} is the coverage-dependent enthalpy of adsorption in kJ mol^{-1}, *R* is the universal gas constant. The adsorption enthalpy at zero loading is calculated according to Supplementary Equation 4.

Supplementary Notes 2. Calculation of adsorption selectivity

The single-component gas isotherms for CO_2, C_2H_2, C_2H_4 and C_2H_6 in Zn-fa-datz (1) and Zn-fa-atz (2) at 298 K were fitted to the dual-site Langmuir-Freundlich equation:

$$q = Q_{A,sat}\frac{b_A P^{v_A}}{1 + b_A P^{v_A}} + Q_{B,sat}\frac{b_B P^{v_B}}{1 + b_B P^{v_B}} \qquad (5)$$

where $Q_{A,sat}$ and $Q_{B,sat}$ is the saturation uptakes (mmol/g) for sites A and B, *P* is the pressure in kPa, b_A and b_B are the affinity coefficients (in kPa^{-vi}) of sites A and B.

The adsorption selectivity of adsorbate *i* relative to adsorbate *j* was established by using the Ideal Adsorption Solution Theory (IAST).[6] The equation is shown in the following:

$$S_{i/j} = \frac{x_i}{x_j}\frac{y_j}{y_i} \qquad (6)$$

here, x_i and x_j are the equilibrium adsorption capacity of components *i* and *j*, respectively, in the adsorbed phase, and y_i and y_j are the mole fractions of components *i* and *j*, in the gas phase.

Supplementary Methods 5. Transient breakthrough experiments vs simulations for Zn-fa-atz (2)

Transient breakthrough experiments were carried out for ternary $C_2H_2/C_2H_4/C_2H_6$ and quaternary $CO_2/C_2H_2/C_2H_4/C_2H_6$ mixtures at a total pressure of 100 kPa and 298 K. Corresponding desorption experiments were also conducted using Helium as purge gas.

Transient breakthrough simulations were carried out for the same set of operating conditions as in the experimental data sets, using the methodology described in earlier publications. [7-11]In these simulations, intra-crystalline diffusion influences are ignored.

Supplementary Methods 6. Pawley and Rietveld refinement of PXRD

The microcrystalline Zn-fa-datz (1) and Zn-fa-atz (2) was placed in a glass capillary (Φ = 0.8 mm) connected with an automatic volumetric sorption apparatus (Micromertics 3FLEX), and heated under high vacuum at 75 °C for 4 hours. After that, CO_2, C_2H_2, C_2H_4 and C_2H_6 gas was introduced by cooling the samples with dry ice-acetone bath to 195K, and the gas dosed volumetrically from calibrated pressure. PXRD data of the gas-loaded samples was collected on a Rigaku SmartLab X-ray powder diffractometer (Cu Kα) with a scanning speed of 0.01 °/step and 7 s/step under capillary transmission mode. All the indexing and refinement were performed by the Reflex plus module of Material Studio 5.0. The pseudo-Voigt profile parameters, background parameters, the cell parameters, the zero point of the diffraction pattern, the global isotropic atom displacement parameters, the Berar-Baldinozzi asymmetry correction parameters, and the March-Dollase preferred orientation correction parameters were optimized step by step to improve the agreement between the calculated and the experimental powder diffraction patterns.

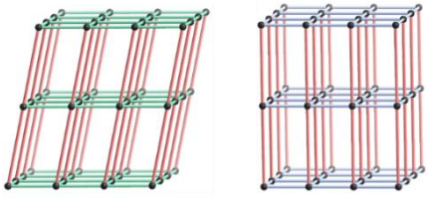

Supplementary Figure 1. Topology of Zn-fa-datz (1) (left) and Zn-fa-atz (2) (right) (dinuclear Zn, triazolate, and dicarboxylate are simplified as black sphere, green or blue stick, and red stick, respectively).

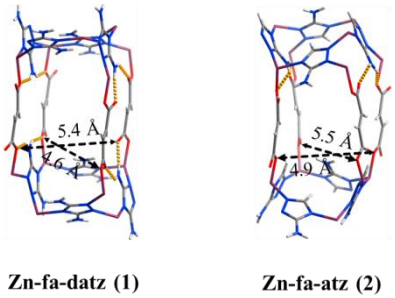

Supplementary Figure 2. The pore size of cage in Zn-fa-datz (1) (left) and Zn-fa-atz (2) (right).

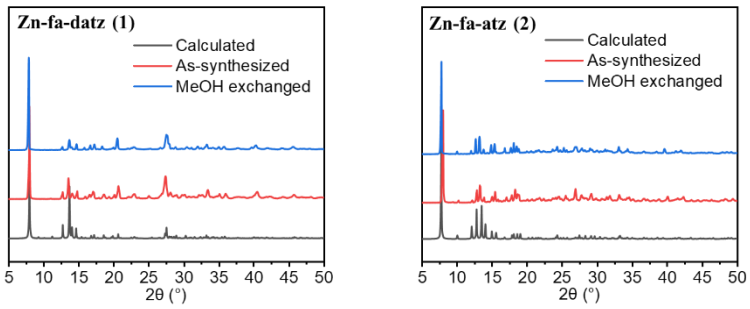

Supplementary Figure 3. PXRD patterns of Zn-fa-datz (1) (left) and Zn-fa-atz (2) (right).

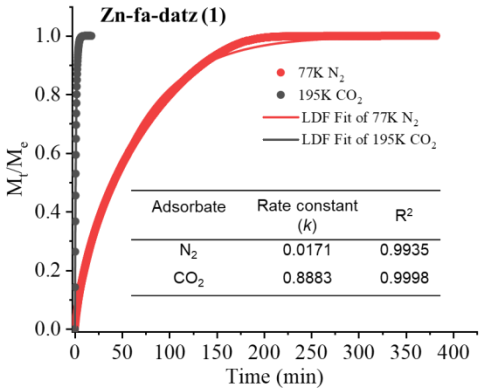

Supplementary Figure 4. Diffusional rate constants of N_2 (77 K) and CO_2 (195 K) in Zn-fa-datz (1).

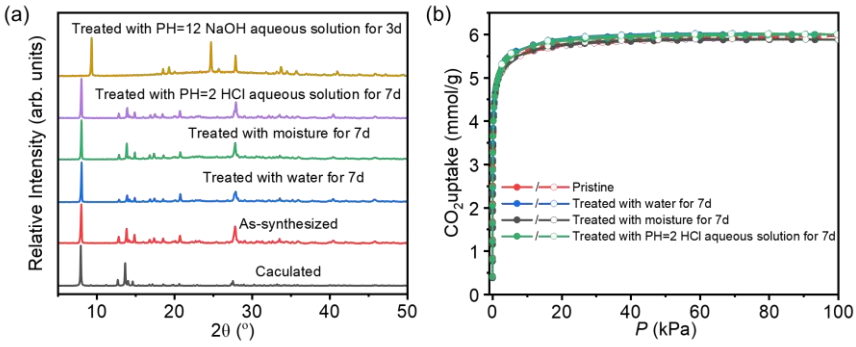

Supplementary Figure 5. PXRD patterns (a) and CO_2 adsorption/desorption isotherms (b) of Zn-fa-datz (1) at 195 K after different treatments. After being exposed to water or moisture (*ca.* 35% RH), or acidic aqueous solutions (pH=2) for 7 days, the PXRD and CO_2 uptakes of the treated samples remain almost unchanged, while obvious change was observed in pH=12 after 3 days, demonstrating the exceptional acid stability but poor alkaline stability of Zn-fa-datz (1).

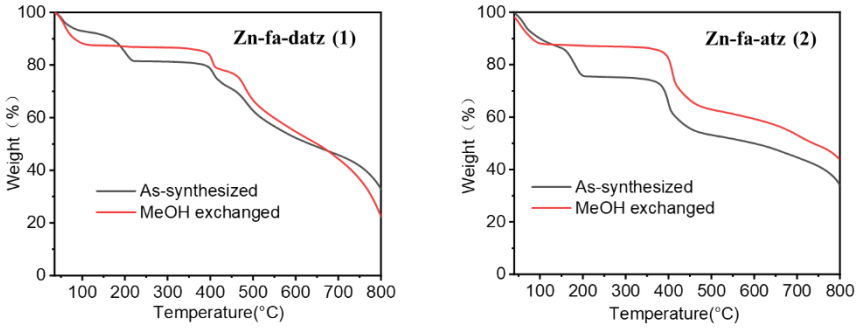

Supplementary Figure 6. TGA curves of Zn-fa-datz (1) (left) and Zn-fa-atz (2) (right).

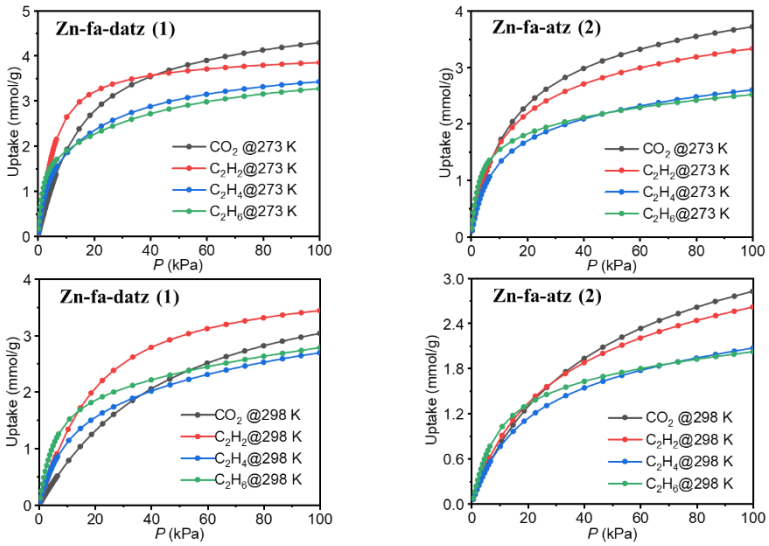

Supplementary Figure 7. Adsorption isotherms of Zn-fa-datz (1) (left) and Zn-fa-atz (2) (right) for CO_2 (black), C_2H_2 (red), C_2H_4 (blue), and C_2H_6 (green) at 273 K and 298 K, respectively.

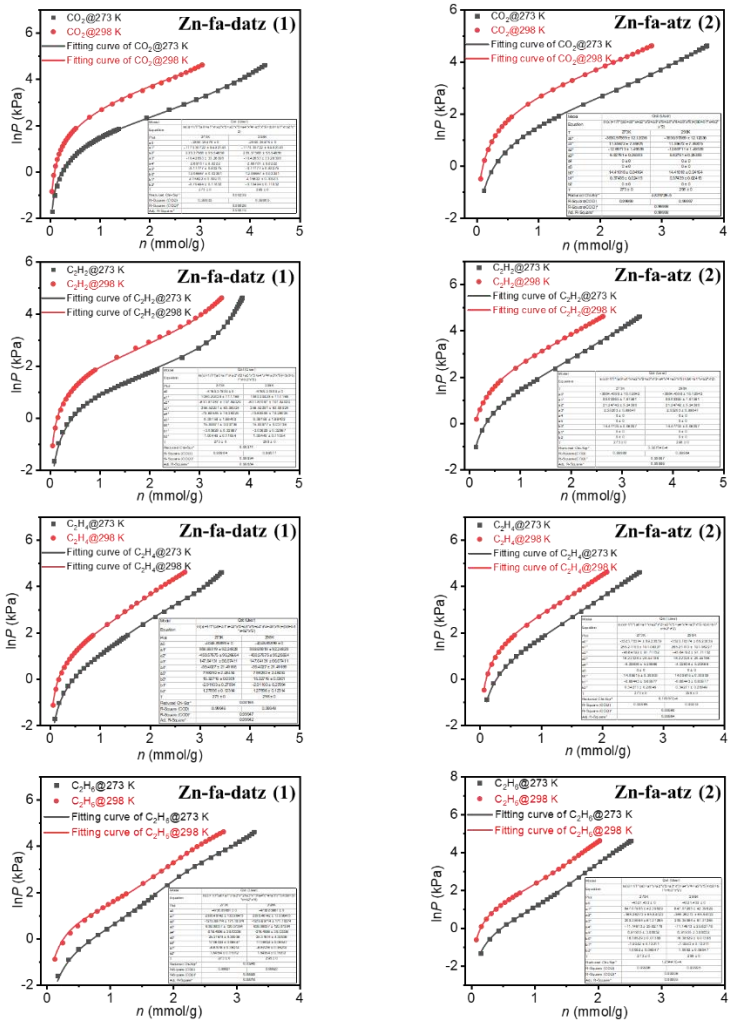

Supplementary Figure 8. Virial fittings of CO_2 , C_2H_2, C_2H_4, and C_2H_6 adsorption isotherms of Zn-fa-datz (1) (left) and Zn-fa-atz (2) (right).

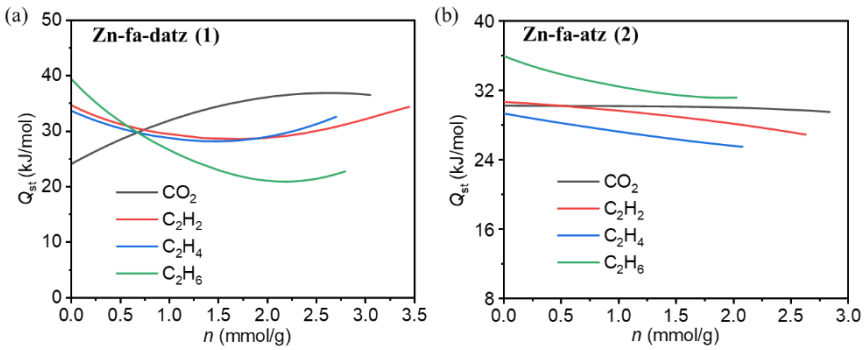

Supplementary Figure 9. Gas adsorption enthalpies of Zn-fa-datz (1) (a), Zn-fa-atz (2) (b) calculated by virial method.

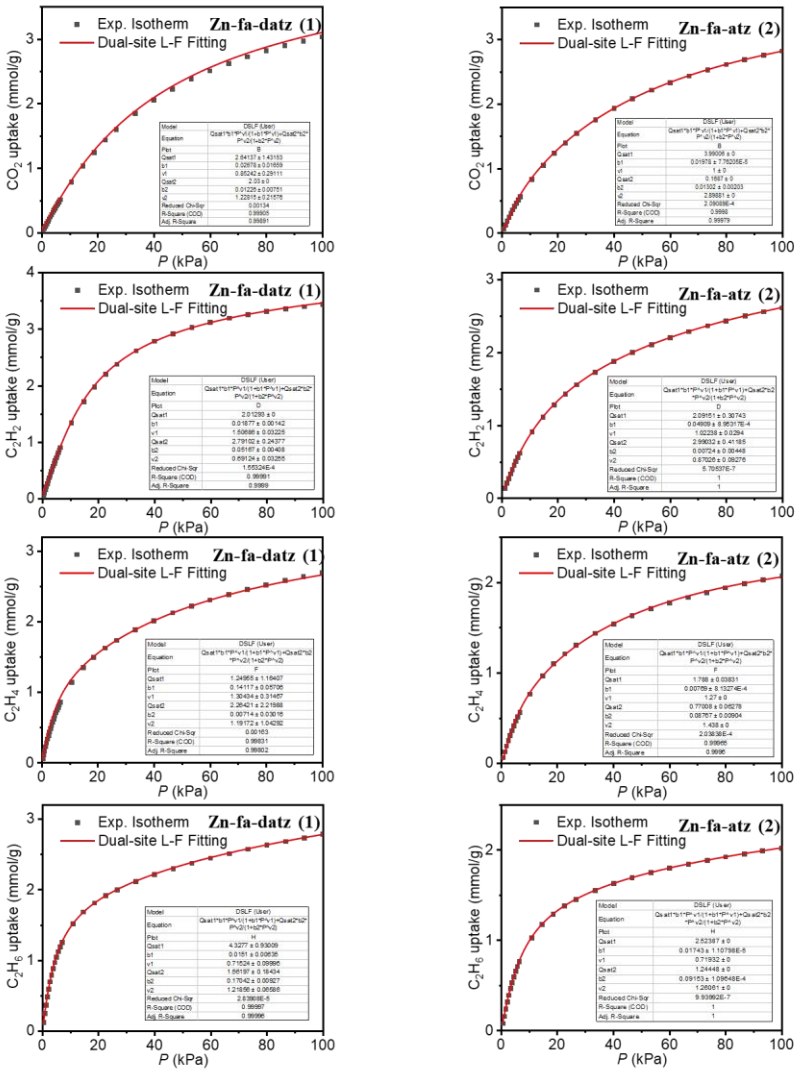

Supplementary Figure 10. Dual-site Langmuir-Freundlich fittings of CO_2, C_2H_2, C_2H_4, and C_2H_6 adsorption isotherms of Zn-fa-datz (1) (left) and Zn-fa-atz (2) (right).

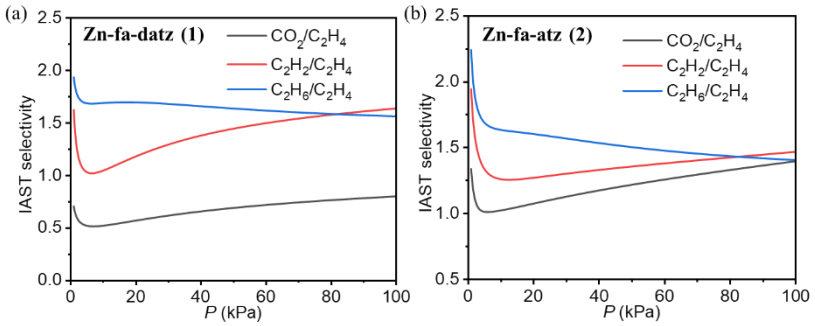

Supplementary Figure 11. Ideal Adsorbed Solution Theory (IAST) selectivities of Zn-fa-datz (1) (a), Zn-fa-atz (2) (b) using the dual-site Langmuir-Freundlich model .

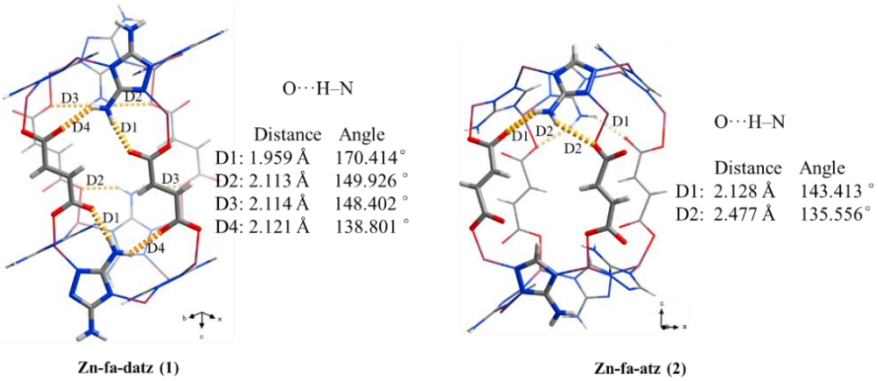

Zn-fa-datz (1) **Zn-fa-atz (2)**

Supplementary Figure 12. The hydrogen bond parameters of Zn-fa-datz (1) and Zn-fa-atz (2).

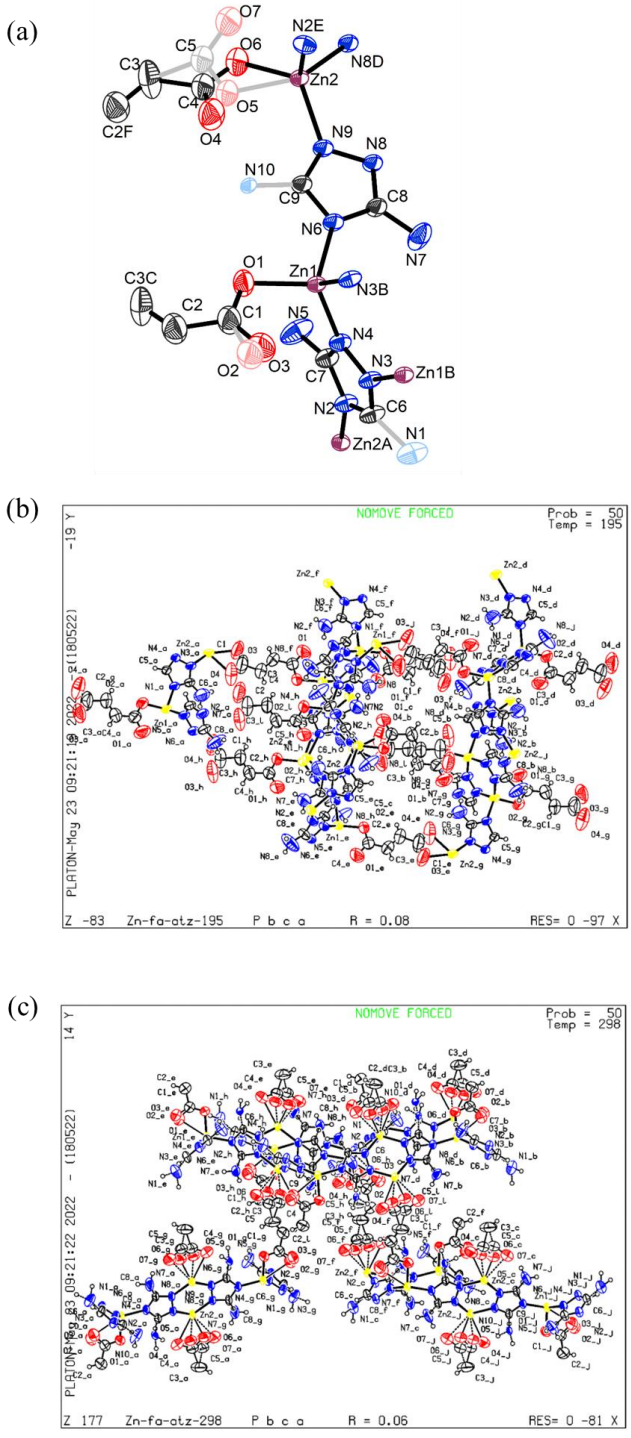

Supplementary Figure 13. Coordination environment of Zn-fa-atz (2). (a) Thermal ellipsoids (30% probability) drawn by Diamond. Hydrogen atoms are omitted for clarity, symmetric codes: A, 1/2-x, -1/2+y, z; B, -x, 1-y, 1-z; C, -1/2+x, y, 1/2-z; D, 1-x, 1-y, 1-z; E, 1/2-x, 1/2+y, z; F, 1/2+x, y, 1/2-z, ORTEP drawing of the Zn-fa-atz (2) of (b) 195 K and (c) 298K, produced by the checkCIF report of the International Union of Crystallography. CCDC deposit number 2176255 and 2176256, respectively.

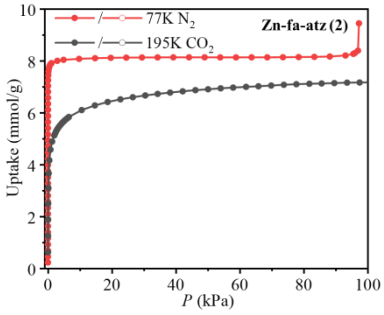

Supplementary Figure 14. Comparison of the adsorption isotherms of 77 K N_2 (red) and 195 K CO_2 (black) for Zn-fa-atz (2).

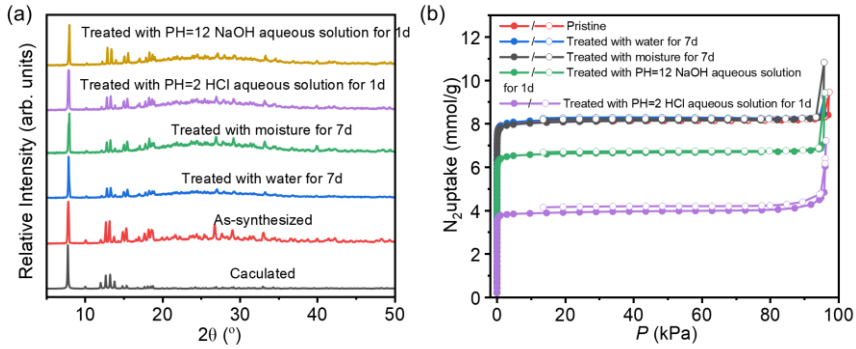

Supplementary Figure 15. PXRD patterns (a) and N_2 adsorption/desorption isotherms (b) of Zn-fa-atz (2) at 77 K after different treatments. After being exposed to water or moisture conditions (*ca.* 35% RH) for 7 days, the PXRD peak intensities and N_2 uptakes of the treated Zn-fa-atz (2) samples remain the same, indicating the exceptional chemical stability of Zn-fa-atz (2) under aqueous and moisture conditions. However, when Zn-fa-atz (2) was exposed to acid (pH=2) or alkaline aqueous (pH=12), the N_2 uptakes of the treated samples dramatically changed after 1 day but the PXRD remain almost unchanged.

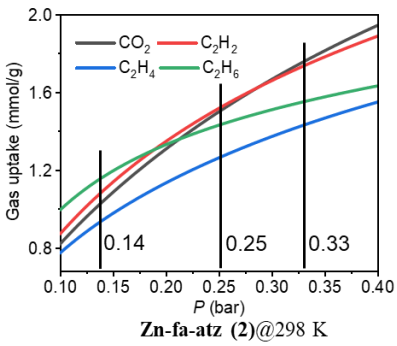

Supplementary Figure 16. Single-component adsorption isotherms of Zn-fa-atz (2) for CO_2 (black), C_2H_2 (red), C_2H_4 (blue) and C_2H_6 (green) from 0.1–0.4 bar and at 298 K obtained from dual-site Langmuir-Freundlich fittings.

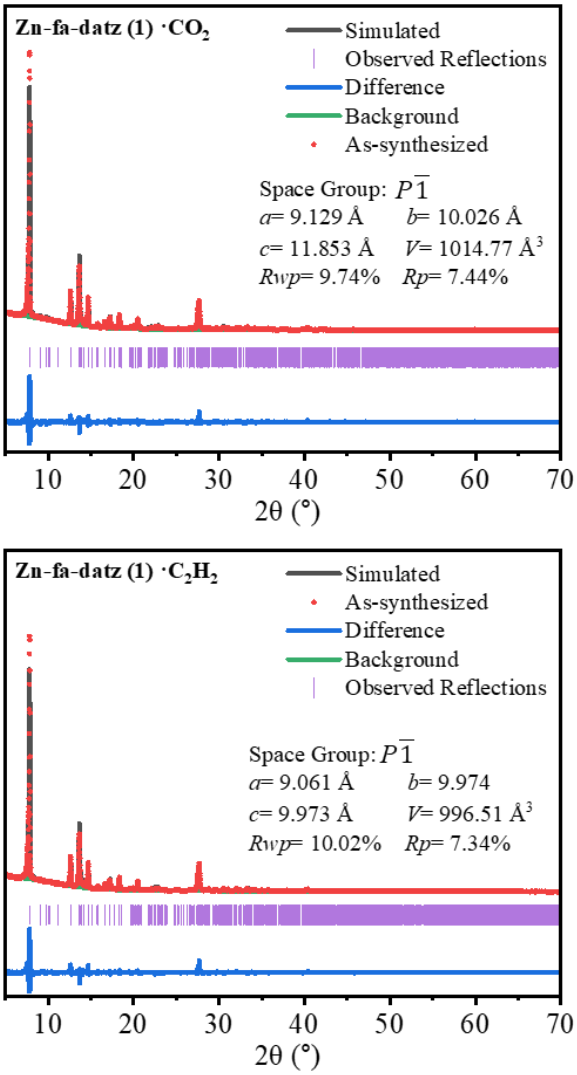

Supplementary Figure 17. Rietveld refinement plots of powder X-ray diffraction data of CO_2-loaded Zn-fa-datz (1) and C_2H_2-loaded Zn-fa-datz (1).

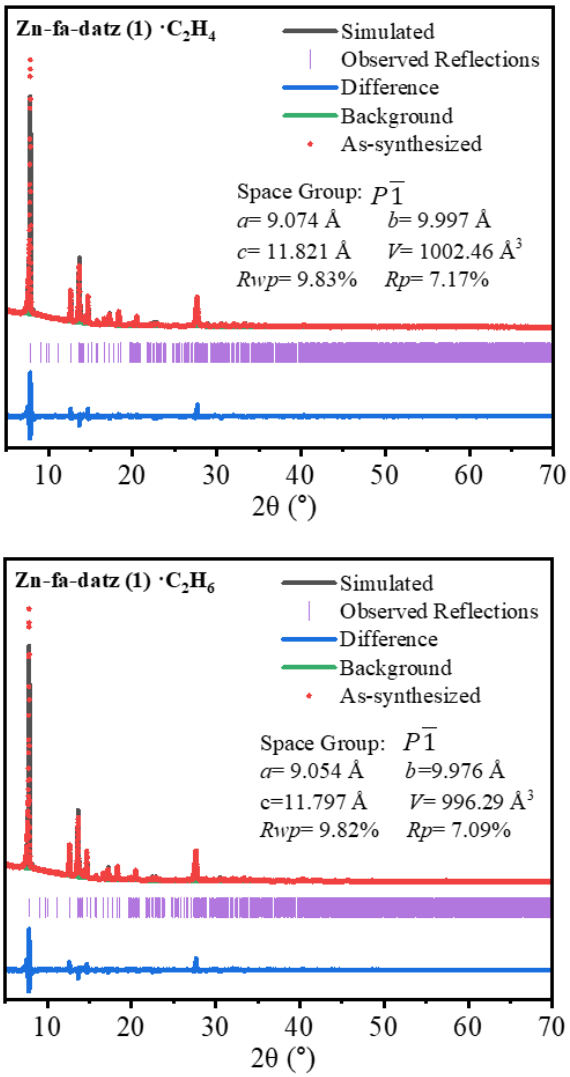

Supplementary Figure 18. Rietveld refinement plots of powder X-ray diffraction data of C_2H_4-loaded Zn-fa-datz (1) and C_2H_6-loaded Zn-fa-datz (1).

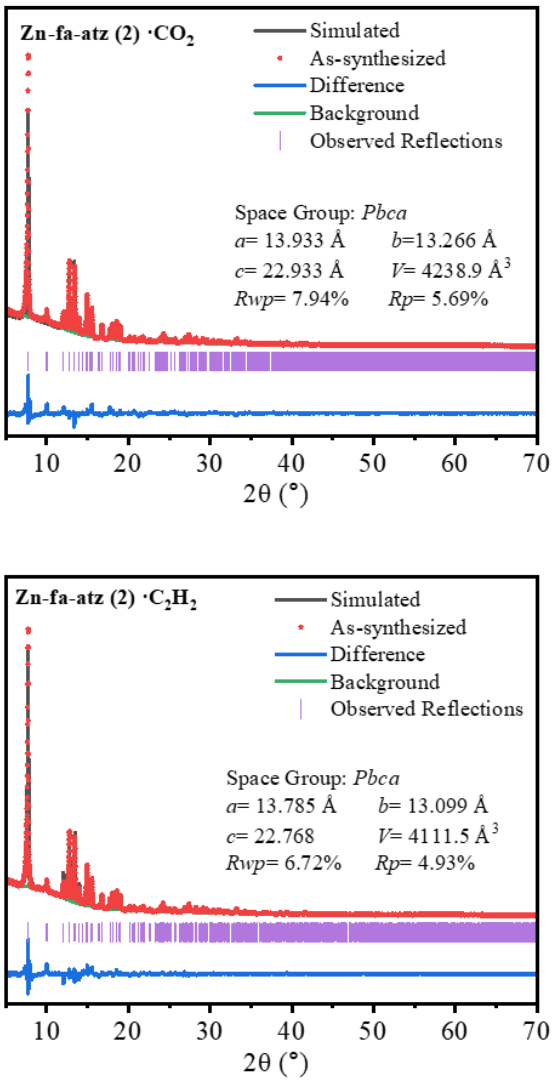

Supplementary Figure 19. Rietveld refinement plots of powder X-ray diffraction data of CO_2-loaded Zn-fa-atz (2) and C_2H_2-loaded Zn-fa-atz (2).

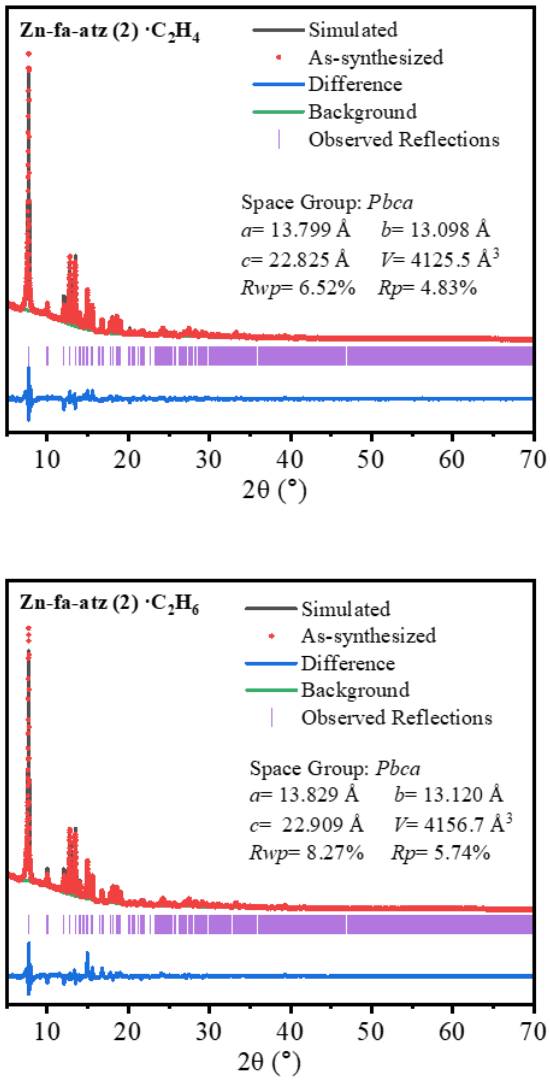

Supplementary Figure 20. Rietveld refinement plots of powder X-ray diffraction data of C_2H_4-loaded Zn-fa-atz (2) and C_2H_6-loaded Zn-fa-atz (2).

Retention time	Components name	Peak area
136.38	C_2H_4	1615.61

Retention time	Components name	Peak area
139.35	C_2H_4	2961.96
139.73	C_2H_6	1.94
140.20	C_2H_2	9.03

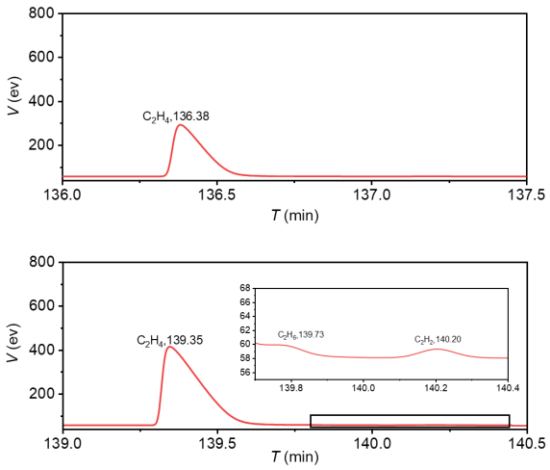

Supplementary Figure 21. GC profiles for C_2H_4 at the outlet of Zn-fa-atz (2) column in a $CO_2/C_2H_2/C_2H_4/C_2H_6$ (1:1:1:1) mixture with a total gas flow of 2 mL/min.

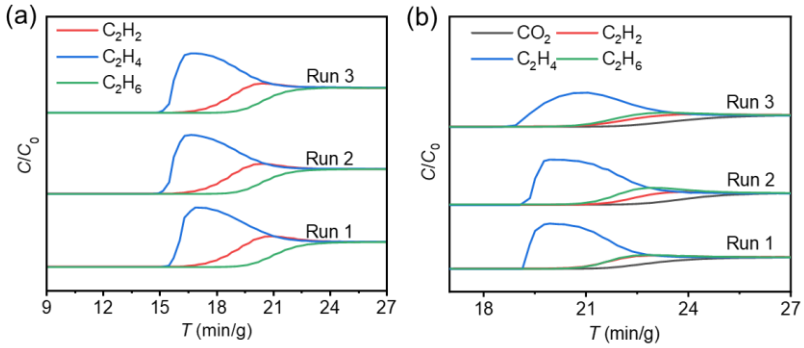

Supplementary Figure 22. Cycling column breakthrough tests of $C_2H_2/C_2H_4/C_2H_6$/He (a), and equimolar $CO_2/C_2H_2/C_2H_4/C_2H_6$ (b) mixture by using Zn-fa-atz (2) at room temperature and 1 atm.

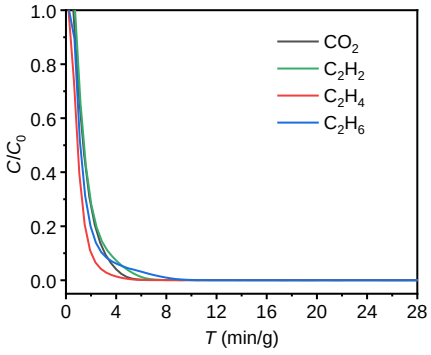

Supplementary Figure 23. Desorption curves of Zn-fa-atz (2) at 70 ^{o}C in He flow with a rate of 20 mL/min.

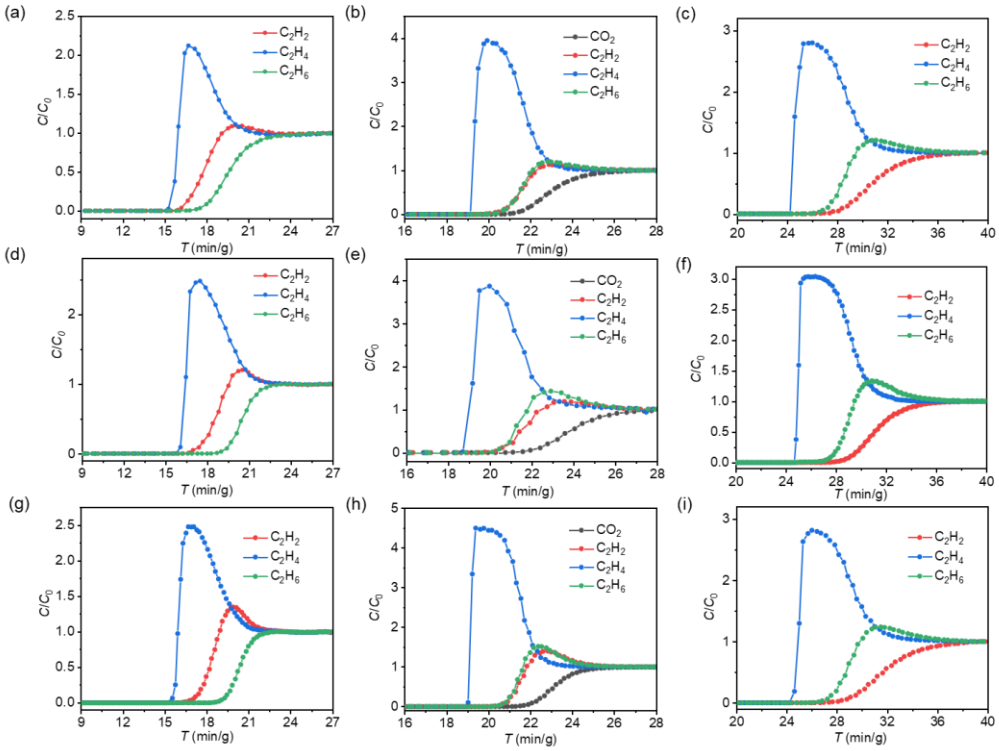

Supplementary Figure 24. Breakthrough curves of Zn-fa-atz (2) with different filling capacities, (a, b, c) the initial batch, (d, e, f) the second batch, (g, h, i) the third batch, using (a, d, g) $C_2H_2/C_2H_4/C_2H_6$/He mixture (1:1:1:4, *v*/*v*/*v*/*v*), (b, e, h) equimolar $CO_2/C_2H_2/C_2H_4/C_2H_6$ mixture (1:1:1:1, *v*/*v*/*v*/*v*) and (c, f, i) $C_2H_2/C_2H_4/C_2H_6$ mixture (1:1:1, *v*/*v*/*v*) at room temperature and 1 atm, respectively.

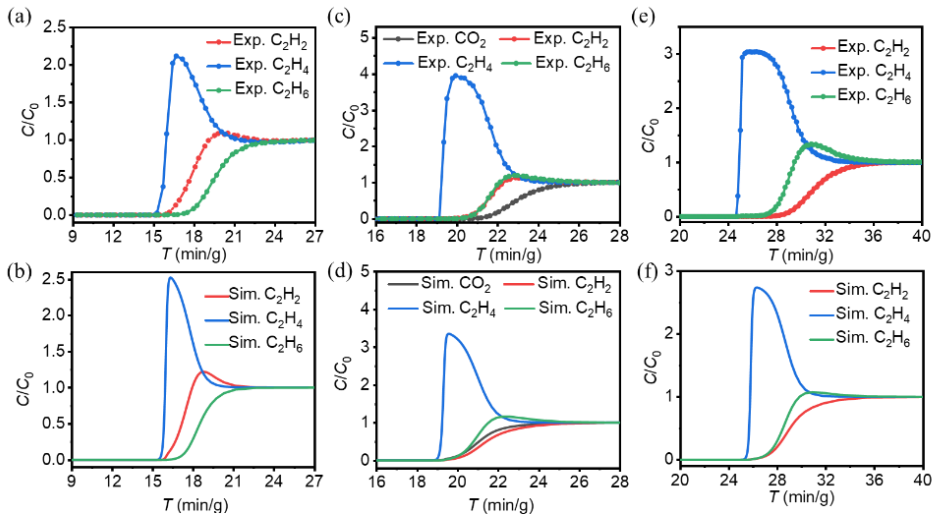

Supplementary Figure 25. Experimental and simulated column breakthrough curves at 298 K of Zn-fa-atz (2) powder for (a, b) $C_2H_2/C_2H_4/C_2H_6$/He, (c, d) $CO_2/C_2H_2/C_2H_4/C_2H_6$ and (e, f) $C_2H_2/C_2H_4/C_2H_6$ separations.

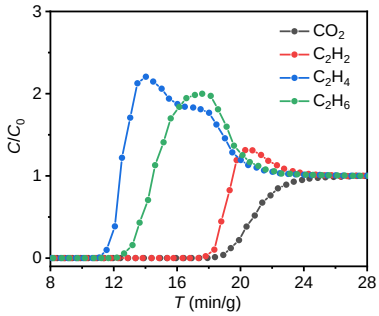

Supplementary Figure 26. Experimental breakthrough curves for quaternary $CO_2/C_2H_2/C_2H_4/C_2H_6$ mixtures (1:1:1:1, *v*/*v*/*v*/*v*) on Zn-fa-atz (2) under wet (*ca.* 36% RH) conditions at room temperature and 1 bar.

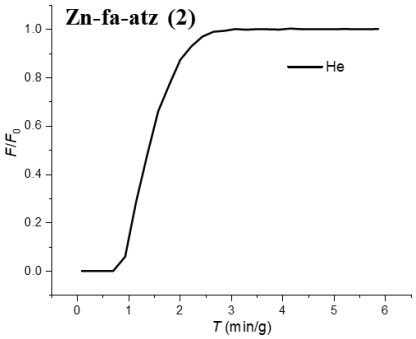

Supplementary Figure 27. Experimental breakthrough curves for He of 2 mL/min in Zn-fa-atz (2) at room temperature and 1 bar.

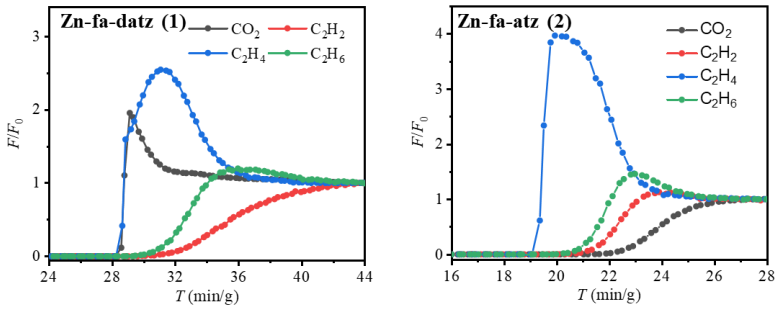

Supplementary Figure 28. Experimental breakthrough curves of Zn-fa-datz (1) and Zn-fa-atz (2) for quaternary $CO_2/C_2H_2/C_2H_4/C_2H_6$ mixtures (1:1:1:1, *v*/*v*/*v*/*v*) with velocity correction.

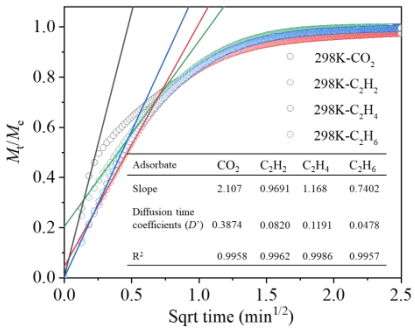

Supplementary Figure 29. Adsorption kinetics profiles (point) and linear fittings (line) of CO_2 (black), C_2H_2 (red), C_2H_4 (blue) and C_2H_6 (green) for Zn-fa-atz (2) at 298 K.

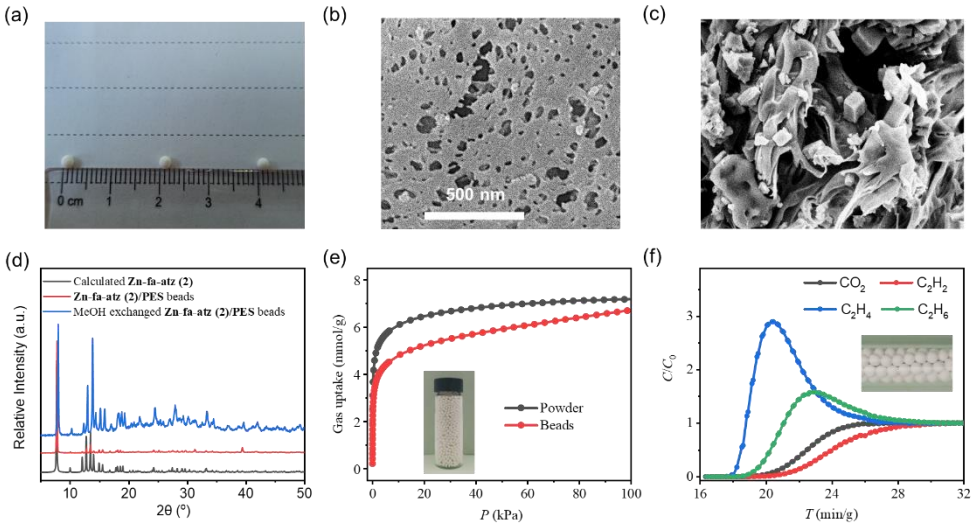

Supplementary Figure 30. (a) Physical appearance image of Zn-fa-atz (2)/PES beads. (b) SEM images of Zn-fa-atz (2)/PES bead surface and (c) the cross-section. (d) PXRD patterns of Zn-fa-atz (2)/PES beads. (e) Comparison of 195 K CO_2 adsorption isotherms of Zn-fa-atz (2) powder and Zn-fa-atz (2)/PES beads. (f) Experimental column breakthrough curves for Zn-fa-atz (2)/PES beads using an equimolar mixture of $CO_2/C_2H_2/C_2H_4/C_2H_6$ under same condition.

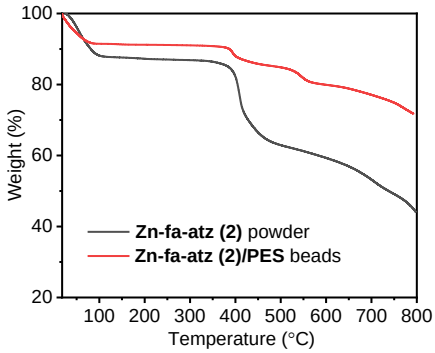

Supplementary Figure 31. Comparison of TGA curves of Zn-fa-atz (2) powder and Zn-fa-atz (2)/PES beads after MeOH exchanged.

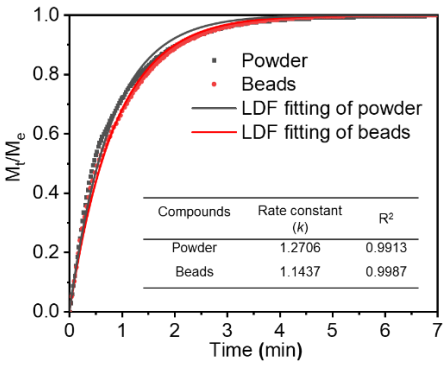

Supplementary Figure 32. Details of diffusional rate constants calculation for Zn-fa-atz (2) powder and Zn-fa-atz (2)/PES beads.

Supplementary Table 1. Summary of the structural information, adsorption data of **Zn-fa-datz (1) and Zn-fa-atz (2)**.

Compound	Zn-fa-atz (2)			Zn-fa-datz (1)	
Temperature	298 K	195 K	77 K	293 K	195 K
Topology	**pcu**			**pcu**	
Pore size[a]		6.3			6.1
Density (g cm^{-3})	1.284	1.336		1.428	
Volume ratio[b]	46.3	42.6		38.9	
Pore volume (measured)[c]	0.361	0.319		0.272	
Pore volume (measured from the uptake of the CO_2 isotherm)[d]		0.285			0.237
Pore volume (measured from the uptake of the N_2 isotherm)[e]			0.283		

[a] Pore size (Å) calculated based on the CO_2 isotherm at 195 K according to the Horvath-Kawazoe model (pore geometry: cylinder). [b] Volume ratio (%) estimated by PLATON software[12] without consideration of the solvent in the pore. [c] The calculated pore volume ($cm^3\ g^{-1}$) estimated from single crystal data using PLATON software. [d] The measured pore volume ($cm^3\ g^{-1}$) calculated from the uptake at P/P_0 = 0.96 assuming the liquid CO_2 filling in the pore. [e] The measured pore volume ($cm^3\ g^{-1}$) calculated from the uptake of the N_2 isotherm at 77 K assuming the liquid N_2 filling in the pore, at P/P_0 = 0.95 for Zn-fa-atz (2).

Supplementary Table 2. Summary of the selectivity and gas adsorption enthalpy data of Zn-fa-datz (1) and Zn-fa-atz (2).

Compounds	Q_{st}[a]				IAST selectivity[b]		
	CO_2	C_2H_2	C_2H_4	C_2H_6	CO_2/C_2H_4	C_2H_2/C_2H_4	C_2H_6/C_2H_4
Zn-fa-atz (2)	30.2	30.6	29.3	35.9	1.4	1.5	1.4
Zn-fa-datz (1)	24.0	34.7	33.6	39.4	0.8	1.6	1.6

[a] Gas adsorption enthalpy (Q_{st}, kJ mol^{-1}). [b] Calculated from IAST theory with a ratio of 50:50 at 298 K and 100 kPa.

Supplementary Table 3. Summary of the single-crystal diffraction data.

Compounds	Zn-fa-atz (2)	Zn-fa-atz (2)	Zn-fa-datz (1)[c]
Empirical formula	$C_8H_8N_8O_4Zn_2$	$C_8H_8N_8O_4Zn_2$	$C_8H_{10}N_{10}O_4Zn_2$
Formula weight	410.96	410.96	441.04
Temperature (K)	298(2)	195(2)	293
Crystal system	orthorhombic	orthorhombic	triclinic
Space group	*Pbca*	*Pbca*	$P\overline{1}$
a (Å)	13.978(8)	13.9330(8)	9.1754(7)
b (Å)	13.376(13)	12.7549(7)	10.0864(7)
c (Å)	22.750(30)	22.9989(12)	11.9515(8)
α (°)	90	90	107.567(6)
β (°)	90	90	101.469(6)
γ (°)	90	90	92.975(6)
V (Å^3)	4253(33)	4087.2(4)	1025.99(13)
Z	8	8	2
D_c (g cm^{-3})	1.284	1.336	1.428
Reflns coll.	4191	3613	
R_{int}	0.0630	0.0796	
R_1 [$I > 2\sigma(I)$][a]	0.0586	0.0792	
wR_2 [$I > 2\sigma(I)$][b]	0.1706	0.2552	
R_1 (all data)	0.0752	0.1020	
wR_2 (all data)	0.1851	0.2728	
GOF	1.057	1.069	

[a] $R_1 = \Sigma||F_o| - |F_c||/\Sigma|F_o|$. [b] $wR_2 = [\Sigma w(F_o^2 - F_c^2)^2/\Sigma w(F_o^2)^2]^{1/2}$. [c] Adopted from ref[13].

Supplementary Table 4. Comparison of C_2H_6/C_2H_4, C_2H_2/C_2H_4 and CO_2/C_2H_4 selectivity in porous materials for one-step C_2H_4 purification for three-component, four-component mixtures at 298 K.

Gas mixtures	Adsorbent	IAST selectivity			References
		C_2H_6/C_2H_4	C_2H_2/C_2H_4	CO_2/C_2H_4	
$C_2H_2/C_2H_4/C_2H_6$	**[Zn(BDC)(H_2BPZ)]**	2.2[b]	1.6[b]	-	[14]
	Zn(ad)(int)	2.4[b]	1.61[a]	-	[15]
	TJT-100	1.2[a]	1.8[a]	-	[16]
	Azole-Th-1	1.46[b]	1.09[b]	-	[17]
	NPU-1	1.32[b]	1.4[b]	-	[18]
	UPC-612	1.4[b]	1.07[b]	-	[19]
	UPC-613	1.5[b]	1.4[b]	-	
	UIO-67-(NH_2)$_2$	1.7[b]	2.1[a]	-	[20]
	Ni-BDC-INA	1.56[b]	1.37[b]	-	[21]
	CPM-173	1.76[b]	1.51[b]	-	
	UiO-66	1.57[b]	1.45[b]	-	
	DMOF-1	1.51[b]	1.35[b]	-	
	CuTiF6-TPPY	2.12[b]	5.47[b]	-	[22]
	ZJNU-115	1.56[b]	2.05[a]	-	[23]
	ZJNU-7	1.56[b]	1.77[a]	-	[24]
	NUM-9a	1.62[b]	1.48[a]	-	[25]
	MIL-125	1.21[b]	2.32[b]	-	[26]
	NH_2-MIL-125	1.18[b]	3.75[b]	-	
	ZSTU-2	1.62[b]	2.36[b]	-	
	LIFM-XYY-6	1.63[b]	1.53[a]	-	[27]
	UPC-66-a	1.65[b]	1.05[b]	-	[28]
	Zn-ATA	1.84[a]	1.81[a]	-	[29]
	HIAM-210	2.0[b]	2.0[b]	-	[30]
	HIAM-326	1.9[b]	1.6[b]	-	[31]
	Zn-fa-datz (1)	1.4[b]	1.5[b]	0.8[b]	**This work**
$C_2H_2/C_2H_4/C_2H_6/CO_2$	**Zn-atz-oba**	1.27[b]	1.43[b]	1.33[b]	[32]
	Al-MOFM$_{15}$[c]	2.51[b]	3.32[b]	-	[33]
	Zn-fa-atz (2)	1.6[b]	1.6[b]	1.4[b]	**This work**

[a] IAST selectivity for 1/99 gas mixture. [b] IAST selectivity for 1/1 gas mixture. [c] IAST selectivity calculated at 293K.

Supplementary Table 5. Host-guest interactions in PXRD analyses and structural refinements of Zn-fa-datz (1) and Zn-fa-atz (2) loaded with CO_2, C_2H_2, C_2H_4 and C_2H_6.

	Zn-fa-datz (1)				Zn-fa-atz (2)			
Guest molecules		H···A (Å)	D-H···A (º)	D···A (Å)		H···A (Å)	D-H···A (º)	D···A (Å)
C_2H_2	C51-H53···N48	2.818	163.268	3.856	C24-H26···N94	3.852	121.854	4.499
	C51-H53···N7	3.825	132.105	4.612				
C_2H_4	C50-H53···N44	1.829	164.048	2.895	C93-H96···N125	3.022	126.05	3.747
	C50-H53···N43	2.251	131.006	3.080	C93-H96···O45	3.277	160.87	4.295
	C50-H53···N45	2.564	134.221	3.416	C92-H95···O3	3.507	121.13	4.157
	C50-H52···N21	2.651	163.689	3.712	C92-H94···O46	3.545	149.50	4.516
	C50-H53···N67	2.682	126.992	3.451	C92-H95···N101	3.584	168.60	4.630
	C50-H53···N48	3.148	127.414	3.909	C93-H97···O67	3.987	124.60	4.691
C_2H_6	C77-H81···N52	1.960	130.758	2.805	C34-H38···N4	1.971	167.94	3.065
	C77-H81···N51	1.998	160.316	3.057	C35-H41···O44	2.137	136.29	3.037
	C77-H79···N28	2.236	149.066	3.230	C34-H36···O15	2.888	148.93	3.883
	C77-H79···N5	2.388	156.829	3.428	C35-H40···N61	3.471	123.23	4.183
	C77-H81···N53	2.395	142.087	3.333	C34-H38···O74	3.938	127.02	4.690
	C78-H84···O65	2.666	144.85	3.622				
	C77-H80···N21	2.751	131.255	3.574				
	C77-H79···N29	2.848	155.325	3.876				
	C77-H80···N60	2.911	141.129	3.831				
	C77-H79···N32	3.329	128.931	4.111				
	C77-H79···N7	3.552	141.687	4.468				
	C78-H83···O16	3.930	142.316	4.848				
CO_2	C98···O1			3.641	C34···O71			3.231
	C98···O2			3.773	C34···O108			3.883
	C98···N7			3.810	O36···C103			3.337
	C98···O3			3.837	O35···C72			3.800
	C98···N14			3.886	O35···C73			3.805
	O99···C3			3.357	O35···C115			3.808
	O99···C6			3.603	O36···C72			3.864
	O99···C5			3.685				
	O99···C4			3.801				
	O97···C3			3.970				

Supplementary Table 6. The adsorption uptake from single-component isotherms and breakthrough time sequence of various gases under different breakthrough conditions for Zn-fa-atz (2).

Gas flow rate (mL/min)		$C_2H_2/C_2H_4/C_2H_6$/He 0.5/0.5/0.5/2	$C_2H_2/C_2H_4/C_2H_6$ 0.5/0.5/0.5	$CO_2/C_2H_2/C_2H_4/C_2H_6$ 0.5/0.5/0.5/0.5
Gas uptake at 298 K (mmol/g)	C_2H_2	1.1[a]	1.7[b]	1.5[c]
	C_2H_4	0.94[a]	1.4[b]	1.3[c]
	C_2H_6	1.2[a]	1.6[b]	1.4[c]
	CO_2			1.5[c]
	uptake sequence	$C_2H_4<C_2H_2<C_2H_6$	$C_2H_4<C_2H_6<C_2H_2$	$C_2H_4<C_2H_6<C_2H_2\approx CO_2$
Breakthrough time sequence	initial	$C_2H_4<C_2H_2<C_2H_6$	$C_2H_4<C_2H_6<C_2H_2$	$C_2H_4<C_2H_6<C_2H_2\approx CO_2$
	2nd	$C_2H_4<C_2H_2<C_2H_6$	$C_2H_4<C_2H_6<C_2H_2$	$C_2H_4<C_2H_6<C_2H_2\approx CO_2$
	3rd	$C_2H_4<C_2H_2<C_2H_6$	$C_2H_4<C_2H_6<C_2H_2$	$C_2H_4<C_2H_6<C_2H_2\approx CO_2$

[a] The single-component gas adsorption uptake data calculated by dual-site Langmuir-Freundlich fittings at partial pressure of 0.14 bar for C2 gases. [b]. The gas uptake data at partial pressure of 0.33 bar. [c] The gas uptake data at partial pressure of 0.25 bar.

Supplementary Table 7. The $CO_2/C_2H_2/C_2H_4/C_2H_6$ breakthrough performances of Zn-fa-datz (1).

Zn-fa-datz (1)	CO_2 uptake (mmol/g)	C_2H_2 uptake (mmol/g)	C_2H_4 uptake (mmol/g)	C_2H_6 uptake (mmol/g)	*S* (C_2H_6/C_2H_4)	*S* (C_2H_2/C_2H_4)	*S* (CO_2/C_2H_4)
Adsorption isotherm at 0.25 bar (298 K)[a]	1.54	2.31	1.69	1.97	-	-	-
Breakthrough experiment	0.52	0.73	0.41	0.63	1.6	1.6	0.8
IAST	-	-	-	-	1.54	1.78	1.27

[a] The single-component gas adsorption uptake data calculated by dual-site Langmuir-Freundlich fittings at partial pressure of 0.25 bar for C2 gases.

Supplementary Table 8. The $CO_2/C_2H_2/C_2H_4/C_2H_6$ breakthrough performances of Zn-fa-atz (2).

Zn-fa-atz (2)	CO_2 uptake (mmol/g)	C_2H_2 uptake (mmol/g)	C_2H_4 uptake (mmol/g)	C_2H_6 uptake (mmol/g)	*S* (C_2H_6/C_2H_4)	*S* (C_2H_2/C_2H_4)	*S* (CO_2/C_2H_4)
Adsorption isotherm at 0.25 bar (298 K)	1.5	1.5	1.3	1.4	-	-	-
Breakthrough experiment at 1 bar (298 K)	0.50	0.46	0.23	0.43	1.87	2.00	2.17
IAST	-	-	-	-	1.4	1.5	1.4

Supplementary References

1. Reid, C. R. & Thomas, K. M. Adsorption of Gases on a Carbon Molecular Sieve Used for Air Separation: Linear Adsorptives as Probes for Kinetic Selectivity. *Langmuir* **15**, 3206-3218 (1999).
2. Lee, C. Y. *et al.* Kinetic separation of propene and propane in metal−organic frameworks: controlling diffusion rates in plate-shaped crystals via tuning of pore apertures and crystallite aspect ratios. *J. Am. Chem. Soc.* **133**, 5228-5231 (2011).
3. Dolomanov, O. V., Bourhis, L. J., Gildea, R. J., Howard, J. A. & Puschmann, H. OLEX2: a complete structure solution, refinement and analysis program. *J. Appl. Crystallogr.* **42**, 339-341 (2009).
4. Sheldrick, G. M. A short history of SHELX. *Acta Crystallogr. A.* **64**, 112-122 (2008).
5. Sheldrick, G. M. Crystal structure refinement with SHELXL. *Acta Crystallogr. C.* **71**, 3-8 (2015).
6. Myers, A. L. & Prausnitz, J. M. Thermodynamics of mixed-gas adsorption. *AIChE J.* **11**, 121-127 (1965).
7. Krishna, R. Metrics for Evaluation and Screening of Metal-Organic Frameworks for Applications in Mixture Separations. *ACS omega* **5**, 16987-17004 (2020).
8. Krishna, R. The Maxwell–Stefan description of mixture diffusion in nanoporous crystalline materials. *Micropor. Mesopor. Mat.* **185**, 30-50 (2014).
9. Krishna, R. Methodologies for evaluation of metal–organic frameworks in separation applications. *RSC Adv.* **5**, 52269-52295 (2015).
10. Krishna, R. Screening metal–organic frameworks for mixture separations in fixed-bed adsorbers using a combined selectivity/capacity metric. *RSC Adv.* **7**, 35724-35737 (2017).
11. Krishna, R. Methodologies for screening and selection of crystalline microporous materials in mixture separations. *Sep. Purif. Technol.* **194**, 281-300 (2018).
12. Spek, A. Single-crystal structure validation with the program PLATON. *J. Appl. Crystallogr.* **36**, 7-13 (2003).
13. Xing, G., Liu, Q., Zhang, Y., Zhang, S. & Dong, Y. Microporous Zinc (II) Metal-Organic Framework with 6-Connected pcu Topology: Synthesis, Structure, and Gas Adsorption Properties. *Z. Anorg. Allg. Chem.* **641**, 1556-1559 (2015).
14. Wang, G. D. et al. One-step C2H4 Purification from Ternary C2H6/C2H4/C2H2 Mixtures by a Robust Metal-Organic Framework with Customized Pore Environment. *Angew. Chem. Int. Ed.* **61**, e202205427 (2022).
15. Ding, Q. et al. One-step Ethylene Purification from Ternary Mixtures in a Metal-Organic Framework with Customized Pore Chemistry and Shape. *Angew. Chem. Int. Ed.* **61**, e202208134 (2022).
16. Hao, H. G. et al. Simultaneous Trapping of C2H2 and C2H6 from a Ternary Mixture of C2H2/C2H4/C2H6 in a Robust Metal-Organic Framework for the Purification of C2H4. *Angew. Chem. Int. Ed.* **130**, 16299 –16303 (2018).
17. Xu, Z. et al. A robust Th-azole framework for highly efficient purification of C2H4 from a C2H4/C2H2/C2H6 mixture. *Nat. Commun.* **11**, 3163 (2020).
18. Zhu, B. et al. Pore Engineering for One-Step Ethylene Purification from a Three-Component Hydrocarbon Mixture. *J. Am. Chem. Soc.* **143**, 1485-1492 (2021).
19. Wang, Y. et al. One-step Ethylene Purification from an Acetylene/Ethylene/Ethane Ternary Mixture by Cyclopentadiene Cobalt-Functionalized Metal-Organic Frameworks. *Angew. Chem. Int. Ed.* **60**, 11350-11358 (2021).
20. Gu, X. W. et al. Immobilization of lewis basic sites into a stable ethane-selective MOF enabling one-step separation of ethylene from a ternary mixture. *J. Am. Chem. Soc.* **144**, 2614-2623 (2022).
21. Zhang, T. et al. General pore features for one-step C2H4 production from a C2 hydrocarbon mixture. *Chem. Commun.* **58**, 4954-4957 (2022).
22. Zhang, P. et al. Synergistic binding sites in a hybrid ultramicroporous material for one-step ethylene purification from ternary C(2) hydrocarbon mixtures. *Sci. Adv.* **8**, eabn9231 (2022).
23. Fan, L. et al. Rational Construction and Performance Regulation of an In(III)–Tetraisophthalate Framework for One-Step Adsorption-Phase Purification of C2H4 from C2 Hydrocarbons. *Inorg. Chem.* **60**, 10819-10829 (2021).
24. Jiang, Z. et al. An aromatic-rich cage-based MOF with inorganic chloride ions decorating the pore surface displaying the preferential adsorption of C2H2 and C2H6 over C2H4. *Inorg. Chem. Front.* **8**, 1243-1252 (2021).
25. Yang, S. Q. et al. Efficient Purification of Ethylene from C2 Hydrocarbons with an C2H6/C2H2-Selective Metal-Organic Framework. *ACS Appl. Mater. Interfaces* **13**, 962-969 (2021).
26. Liu, P. et al. Construction of saturated coordination titanium-based metal–organic framework for one-step C2H2/C2H6/C2H4 separation. *Sep. Purif. Technol.* **276**, 119284 (2021).

27. Xiong, Y. Y. et al. Dynamic Spacer Installation of Multifunctionalities into Metal–Organic Frameworks for Spontaneous One-Step Ethylene Purification from a Ternary C2-Hydrocarbons Mixture. *CCS Chem.* 023.202302698 (2023).
28. Wang, Y. T. et al. Guest-molecule-induced self-adaptive pore engineering facilitates purification of ethylene from ternary mixture. *Chem* 8, 3263–3274 (2022).
29. Ding, Q. et al. One-step ethylene purification from ternary mixture by synergetic molecular shape and size matching in a honeycomb-like ultramicroporous material. *Chem. Eng. J.* **450**, 138272 (2022).
30. Liu, J., Wang, H. & Li, J. Pillar-layer Zn-triazolate-dicarboxylate frameworks with a customized pore structure for efficient ethylene purification from ethylene/ethane/acetylene ternary mixtures. *Chem. Sci.* **14**, 5912-5917 (2023).
32. Cao, J. W. et al. One-step ethylene production from a four-component gas mixture by a single physisorbent. *Nat. Commun.* **12**, 6507 (2021).
33. Laha, S. et al. Tailoring Robust Al-MOF for Trapping C2H6 and C2H2 towards Efficient C2H4 Purification from Quaternary Mixtures. *Chem. Sci.* **13**, 7172-7180 (2022).